

2. EXPLANATORY NOTES¹

Shipboard Scientific Party²

INTRODUCTION

The “Explanatory Notes” chapter documents the procedures and methods employed in the various shipboard laboratories during Leg 209. This information concerns only shipboard methods described in the Leg 209 *Initial Reports* volume of the *Proceedings of the Ocean Drilling Program* (ODP). Methods for shore-based analysis of Leg 209 samples and data will be described in the individual scientific contributions to be published in scientific journals and in the Leg 209 *Scientific Results* volume.

Authorship

All shipboard scientists contributed to the completion of this volume. The separate sections of the chapters were, however, written by groups of scientists as given below (listed alphabetically):

Leg Summary: Shipboard Scientific Party
Background and Objectives: Kelemen, Kikawa
Operations: Miller, Storms
Igneous Petrology: Abe, Cipriani, Meurer, Seyler, Takazawa
Metamorphic Petrology: Bach, Garrido, Harvey, Paulick, Rosner
Structural Geology: Casey, Cheadle, Dick, Faul, Schroeder
Geochemistry: Chambers, Godard, Graham
Physical Properties: Carlson, Ildelfonse
Paleomagnetism: Garces, Gee
Microbiology: Griffin, Josef
Downhole Measurements: Iturrino

¹Examples of how to reference the whole or part of this volume.

²Shipboard Scientific Party addresses.

Numbering of Sites, Holes, Cores, and Samples

Drilling sites are numbered consecutively from the first site drilled by the *Glomar Challenger* in 1968. At a site, multiple holes can be drilled by removing the drill pipe from the seafloor, moving the ship a short distance, and then drilling a new hole. For all ODP drill sites, a letter suffix distinguishes each hole drilled at the same site. The first hole drilled is assigned the site number modified by the suffix "A," the second hole takes the site number and suffix "B," and so forth.

The cored interval is measured in meters below seafloor (mbsf). The depth below seafloor is determined by subtracting the water depth estimated from the initial drill pipe measurement, which gives the length of pipe from the rig floor to the seafloor (measured in meters below rig floor [mbrf]), from the total drill pipe measurement. During most ODP cruises, each cored interval is generally 9.5–9.6 m long, which is the length of a core barrel. However, one potential cause of poor recovery in hard rock coring is core jamming in the bit or the throat of the core. To enhance recovery, most cored intervals during Leg 209 were reduced to 4.5–5 m (half cores). A recovered core is divided into 1.5-m sections that are numbered serially from the top. When full recovery is obtained, the sections are numbered sequentially as recovered starting with 1 at the top of the core; the last section may possibly be shorter than 1.5 m (Fig. F1).

When the recovered core is shorter than the cored interval, the top of the core is equated with the top of the cored interval (in mbsf) by convention to achieve consistency in handling analytical data derived from the cores. Samples removed from the cores are designated by distance measured in centimeters from the top of the section to the top and bottom of each sample removed from that section. A full identification number for a sample consists of the following information: leg, site, hole, core number, core type, section number, piece number (for hard rock), and interval in centimeters measured from the top of section. For example, a sample identification of "209-1268A-2R-2, 30–32 cm" would represent a piece of core removed from the interval between 30 and 32 cm below the top of Section 2, Core 2 (R designates that this core was taken with the rotary core barrel) of Hole 1268A from Leg 209 (Fig. F1).

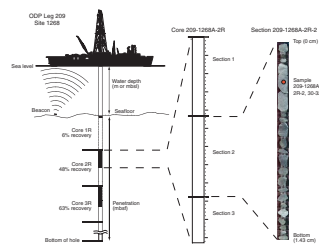
In rare cases, coring intervals were repeated when the bit failed to reach the bottom of the hole after a core was recovered. Since the rock recovered in these instances represented no new penetration, the core designator "M" was assigned. Cores recovered with the logging-while-coring assembly were assigned the core designator "A."

Core Handling

At the start of coring operations, we elected not to use plastic liners in the core barrels because of concern that fragments of core might jam in the liner, thus limiting recovery. During operations at Site 1272, we recovered a few cores with plastic liners and noted higher average recovery than we had achieved without liners in similar lithologies. All cores recovered at Sites 1273, 1274, and 1275 were therefore collected in plastic liners.

For cores recovered without plastic liners, core pieces were transferred to clean, labeled split core liners in the core splitting room. The top of the core was marked with a blue liner cap, and colorless liner caps were glued to the bottom of liner sections. When cores were recov-

F1. ODP sample labeling scheme, p. 42.



ered in plastic liners, liner caps (blue = top) were glued onto liner sections on the catwalk after splitting the liner into 1.5-m sections. The 1.5-m sections were transferred to the core splitting room, where the plastic liners were split lengthwise.

Nearly all pieces were marked with a red wax pencil before they were extracted from the core barrel or removed from the split core liner to preserve orientation. In some cases, the pieces were too small to be certain of orientation. Therefore, the red wax mark does not universally indicate that the core piece was oriented.

Pieces of the core were pushed together and the length of the core in each split core liner was measured to the nearest centimeter; this measurement was entered into the ODP curation data acquisition program. Whole-round samples for microbiology were sampled in the core splitting room prior to any other handling using techniques described in [“Microbiology,”](#) p. 24.

Core pieces that could be fit along fractures were curated as single pieces with letter suffix designations as subpieces. A plastic spacer was secured to the split core liner with acetone between individual pieces and/or reconstructed contiguous groups of pieces. These spacers may represent a substantial interval of no recovery.

The length of each section of core including spacers was entered into the curation database as the curated length. The curated length will commonly differ by a few centimeters from the liner length measured on the catwalk. Subsequently, the cores were marked by a structural geologist to indicate a split line, ideally maximizing the expression of dipping fabric (i.e., perpendicular to foliation) on the cut face of the core. The outer cylindrical surfaces of the whole-round pieces were scanned with the ODP digital core scanner, using the split line marking for registration. Each section was scanned using the shipboard multisensor track (MST) (see [“Nondestructive Tests,”](#) p. 18, in [“Physical Properties”](#)). Each piece of core was then split into archive and working halves, with the positions of spacers maintained for both halves. Pieces are numbered sequentially from the top of each section, beginning with number 1; reconstructed groups of pieces are assigned the same number but are lettered consecutively. Pieces are labeled only on the outer cylindrical surfaces of the core. If the piece is oriented, an arrow is added to the label pointing to the top of the section.

The archive half of each core was described, and observations were recorded on ODP templates and spreadsheets developed by the shipboard scientific party (for details see individual disciplinary sections in this chapter). Digital images of the archive halves were made on the ODP digital imaging system. Archive-half sections were also passed through the cryogenic magnetometer for magnetic remanence measurements. Finally, the archive half was photographed using black-and-white and color film. Close-up photographs (color and black and white) were taken of particular features for illustrations in the summary of each site, as requested by individual scientists.

The working half of the core was sampled for both shipboard and shore-based laboratory studies. Samples were routinely taken for shipboard physical properties; paleomagnetic, thin section, and geochemical analyses; and microbiological and molecular investigations, as described in the sections to follow. Each extracted sample was logged into the sampling database program by the location and the name of the investigator receiving the sample or by the type of shipboard sample. Records of all removed samples are kept by the curator at ODP. The extracted samples were sealed in plastic vials, cubes, or bags and labeled.

Following the shipboard initial scientific measurements and sampling, both halves of cores were shrink-wrapped in plastic to prevent rock pieces from moving out of sequence during transit. The working and archive halves of cores were then put into labeled plastic tubes, sealed, and transferred to cold-storage space aboard the drilling vessel. At the end of Leg 209, the cores were transferred from the ship to cold storage at the ODP Repository in Bremen, Germany.

IGNEOUS PETROLOGY

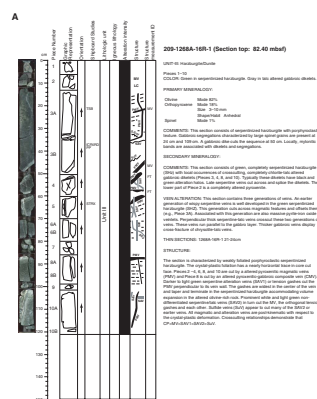
Hard rock petrographic observations made during Leg 209 are stored in both written and electronic media. All igneous descriptions and measurements were made on the archive halves of the cores, except where otherwise noted. The igneous team worked together during the same shift to minimize measurement inconsistencies. Each member of the team was responsible for making a specific set of observations throughout the entire core. Some of the igneous observations obtained during shipboard analyses of core are summarized in the visual core description (VCD) forms (Fig. F2). Complete macroscopic descriptions are available for each site in igneous petrology spreadsheets (see the “**Supplementary Material**” contents list). The depth of a given feature was defined as the point where the center of a given structure intersects the center of the cut face of the archive half of the core or, if the feature does not appear in the center of the core, the depth of the centroid of the feature in the archive half of the core. All descriptive parameters are converted to numerical equivalents and are detailed fully in the spreadsheets. In the case of the rock name (e.g., dunite) the numbers are simply shorthand. For more quantitative descriptions (e.g., crystal shape), the numerical system defines progressive sequences (e.g., equant to elongate) and intermediate values (e.g., 1.5) are used to characterize intermediate stages (see the “**Supplementary Material**” contents list). Complete microscopic descriptions on petrographic thin sections are available for each site in the “**Thin Sections**” (see the “**Core Descriptions**” contents list).

Rock Classification

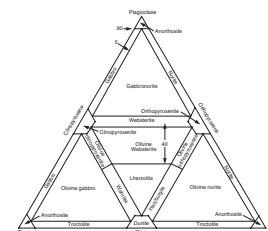
Characterization of igneous rocks is based on abundance of primary minerals, grain size, and texture. When modal analyses can be reliably obtained, igneous rocks are classified according to the Streckeisen (1974) classification, as shown in Figure F3. A sample that contains >10% chromian spinel is called “chromitite.”

Rock names are assigned based on the primary phases present prior to alteration. For severely altered rocks, the term “primary assemblage” is used to refer to the estimated pre-alteration mineral assemblage. Where alteration in ultramafic rocks is so extensive that estimation of the primary phase assemblages is not possible, the protolith is called “serpentinite.” If primary assemblages, their pseudomorphs, and textures can be recognized in ultramafic samples, even though they were partially or completely replaced, the rock name used is based on the reconstructed primary assemblage and is termed either “serpentinized” or “altered” (i.e., serpentinized dunite, altered lherzolite, etc.).

F2. Example VCD and symbols, p. 43.



F3. Modal classification of igneous rocks, p. 45.



Primary Minerals

The primary rock-forming minerals recovered are olivine, orthopyroxene, clinopyroxene, spinel, Fe-Ti oxide, plagioclase, and amphibole. For each, the following data are available for each site on the VCDs (see the “**Core Descriptions**” contents list):

1. Visually estimated modal percent of the primary original minerals;
2. Minimum, maximum, and average grain size; and
3. Crystal shape or habit.

In addition, accessory phases such as mica, other oxide minerals, sulfide minerals, or others (e.g., zircon) are also noted and the above three classes of observations collected. The modal percentage of the mineral includes both the fresh and altered parts of the rocks interpreted to represent that mineral. Grain size refers to the average long dimension of the minerals and is given in millimeters, as are the minimum and maximum crystal sizes. The shape describes the aspect ratio of the grains and is used when deformation has modified the original crystal morphology. The aspect ratio is the ratio of the short to the long dimension of the crystal. The terms euhedral, subhedral, anhedral, and interstitial are used to describe the shapes of crystals interpreted to preserve their igneous morphology. The shapes are divided into four classes:

1. Equant: aspect ratio = less than 1:2.
2. Subequant: aspect ratio = 1:2 to 1:3.
3. Tabular: aspect ratio = 1:3 to 1:5.
4. Elongate: aspect ratio = more than 1:5.

Spinel occurs in various shapes that can be divided into three categories:

1. Equant: the shape is equidimensional with flat and/or curved surfaces.
2. Interstitial: a transitional category between vermicular and equant. The outer surfaces of these spinels are often concave outward and have thin tips departing from the corner of the grain.
3. Vermicular: has intricate shape forming symplectitic intergrowths with pyroxenes and/or olivine.

The presence of linear arrays of spinel grains, termed trains, that sometimes form in peridotite is denoted simply by yes (1) or no (0), and their character is described more fully in the comments. In general, these descriptions and estimates are based on hand-sample inspection; however, a limited sample suite was also studied in petrographic thin sections, and these observations were used to refine the hand-sample descriptions. This is indicated in the Shipboard Studies column of the VCD forms.

Igneous Texture and Structure

Five major classes of rocks (peridotite, pyroxenite, gabbro, diabase, and basalt) are delineated for their igneous texture. For peridotites and pyroxenites, descriptors include the following:

1. Coarse granular: grain size is uniform and >1.0 cm.
2. Medium granular: grain size is uniform at 0.3–1.0 cm.

3. Porphyroclastic: relatively large crystals are surrounded by a fine-grained matrix.
4. Porphyroclastic elongated: porphyroclasts are elongated.

For diabase and gabbroic rocks the texture is defined by the grain size and the extent of igneous foliation that is developed. Diabases have grain sizes that range from too small to be discerned by the unaided eye to fine grained; microgabbros are fine grained; gabbros are medium grained or coarser. The textural distinction between diabases and microgabbros is based on the modal homogeneity of the sample. Diabases are defined as having a felty texture with randomly distributed plagioclase laths throughout and are modally homogeneous. Microgabbros can have felty textured plagioclase or be more massive, but those with a felty texture have distinctive modal segregations of plagioclase laths into a framework in the sample. For basaltic rocks, the proportions and characters of phenocrysts and vesicles define the following textures:

1. Aphyric: phenocrysts occupy <1%.
2. Porphyritic: phenocrysts (>1%) are surrounded by finer-grained groundmass.
3. Seriate: the crystals of the principal minerals show a continuous range of sizes.
4. Poikilitic: relatively large crystals of one mineral "oikocryst" enclose smaller crystals of one or more other minerals ("chadacrysts").
5. Glomerocrystic: a porphyritic texture where the phenocrysts are clustered.
6. Vesicular: vesicles occupy >10%.

Segregations/Dikes/Veins

We use the term "dike" to refer to any later crosscutting feature that formed by injection of magma and/or juvenile fluids and reserve the word "vein" for describing features formed by precipitation from non-magmatic fluids. Veins are described in "[Metamorphic Petrology](#)," p. 7.

Thin Section Description

Thin sections of igneous rocks complement hand-specimen observations. In general, the same type of data was collected from thin sections as from visual descriptions but the microscopic analyses provide a more complete and accurate description of the rock. Modal data were collected from representative thin sections by visual estimates. All data for each site are available in "Thin Sections" (see the "[Core Descriptions](#)" contents list). Rigorous reconstruction of peridotite primary assemblages was not possible on board ship because they require additional information such as the bulk rock and mineral chemistry for each sample. Therefore, we reported only the abundance of serpentine after olivine and pyroxene. Additional textural features recorded include crystal sizes (measured using a micrometer scale); the presence of inclusions, overgrowths, and zonation; and the presence of accessory minerals.

METAMORPHIC PETROLOGY

Metamorphic characteristics of the drill core were determined using visual core descriptions (macroscopic and mesoscopic), microscopic thin section descriptions, and X-ray diffraction (XRD) analyses. Metamorphism, metasomatism, and hydrothermal alteration are used loosely and synonymously without making implications about open- vs. closed-system behavior. For each piece of core the following information was recorded: leg, site, hole, core number, core type, section number, piece number (consecutively downhole), and position in the section. All metamorphic descriptions and measurements were made on the archive halves of the cores, except where otherwise noted. The depth of a given feature was defined as the point where the center of a given structure intersects the center of the cut face of the archive half of the core or, if the feature does not appear in the center of the core, the depth of the centroid of the feature in the archive half of the core. The metamorphic petrology group worked together during the same shift to minimize measurement inconsistencies. Each member of the team was responsible for making a specific set of observations throughout the entire core.

The visual core descriptions provide information (on a piece-by-piece basis) on the extent of replacement of igneous minerals by secondary minerals, as well as the nature and approximate modes of secondary mineral assemblages. These data are used to estimate the total extent of rock alteration that is reported for each site in the alteration log (see the “[Supplementary Material](#)” contents list). Further, the extent to which metamorphic minerals contribute to any subsolidus fabric is recorded in the comments. Alteration styles are background, patchy, and vein halos. The presence of veins is noted in the alteration log, and detailed vein descriptions and vein abundance estimates are provided in the vein log, which records style, mineralogy, shape, and connectivity of veins (see the “[Supplementary Material](#)” contents list). Thin section descriptions and XRD results were integrated with visual core descriptions to ensure internal consistency and maximize accuracy of the core descriptions.

Visual Core Descriptions

The metamorphic mineral assemblages as well as style and intensity of alteration were recorded in the alteration log. Primary phases (olivine, clinopyroxene, orthopyroxene, spinel, and plagioclase) and the secondary minerals that replace them were noted and, where possible, the volume percent of each phase was estimated in hand specimen and confirmed by observation of representative thin sections. In the alteration log, there is one entry for each piece, unless pyroxenite or gabbro dikes/segregates are developed, in which case their metamorphic characteristics were logged separately. Pervasively altered, calcium-metasomatized rocks are called rodingites if the alteration has destroyed the primary igneous composition and textural relationships. Similarly, pervasively serpentinized rocks with unknown protolith are named serpentinite. If the nature of the protolith can be established, the adjective serpentinized or rodingitized is added to the rock name. Alteration intensity is classified as follows:

1. Fresh = <2%.
2. Slight = 2%–10%.

3. Moderate = 10%–40%.
4. High = 40%–80%.
5. Very high = 80%–95%.
6. Complete = >95%.

This estimated alteration intensity is added to the rock name (e.g., completely serpentinized harzburgite, highly altered metagabbro, etc.). In addition, the estimated alteration intensity was recorded in the alteration log as percentage values. The alteration mineralogy was tentatively described (and confirmed by thin section and XRD) and the degree of alteration of each primary phase was recorded in percent. The proportions of phases in the alteration assemblage replacing olivine, orthopyroxene, clinopyroxene, and plagioclase were estimated and reported normalized to 100%. In some instances, it is appropriate to distinguish between pseudomorph and nonpseudomorph alteration styles, in which case this was noted in the comments (e.g., bastite after orthopyroxene preserved kink banding). Both alteration styles are pervasive but pseudomorph indicates that primary features of the protolith are preserved, whereas nonpseudomorph indicates these were destroyed. Replacement textures (e.g., coronas, overgrowths, and pseudomorphs) were also recorded in the comments.

Vein mineralogy and mineral abundance, the top and the bottom location of the vein in the piece(s), vein type, shape, connectivity, structure, texture, color, and associated vein halos were recorded in the vein log. The criteria for distinguishing different vein types (paragranular and transgranular), vein shapes (straight, sigmoidal, kinked, and irregular), connectivities (single, branched, and network), textures (cross-fiber, slip-fiber, massive, and vuggy), and structures (simple, composite, and banded) are outlined in Table T1 and illustrated in Figure F4. For an individual piece, multiple entries were made in the vein log if several vein types are developed. The length and width of each vein as well as its orientation were measured by the structural geology group. The percent area of the veins within a piece or interval was estimated visually. These data were used to calculate the volume percentage of each vein type within a given interval and within the entire core.

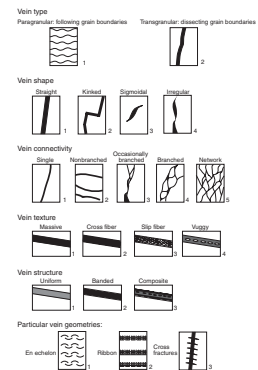
Acronyms used in the alteration and vein logs and in the thin section description forms are listed in Table T2. We used number schemes (see Fig. F4) to enter vein descriptions in the vein logs. If a vein could not be appropriately characterized using this classification, we marked it “mixed” (number 9) and entered a description in the comments.

Thin Section Descriptions

Detailed petrographic thin section descriptions were made to aid in identification and characterization of metamorphic and vein mineral assemblages. Stable mineral parageneses were noted, as were textural features of minerals indicating overprinting events (e.g., coronas, overgrowths, and pseudomorphs). Secondary mineral assemblages and replacement relations to primary phases were described, and secondary modes were estimated visually. The nature of minor and trace phases (carbonates, sulfides, and oxides) as well as the extent of Cr spinel alteration could usually not be established by visual core description. Particular emphasis was therefore placed on the identification and description of minor and trace phases. The area of a thin section occupied by different vein types and relationships between veins and rock alteration were also recorded. These data are summarized, together with igneous

T1. Metamorphic petrology terms, p. 59.

F4. Description of metamorphic veins, p. 46.



T2. List of mineral acronyms, p. 60.

and structural descriptions, in the thin section description sheets (see the “**Core Descriptions**” contents list). The modal estimates allowed characterization of the intensity of metamorphism and aided in establishing the accuracy of the macroscopic and microscopic visual estimates of the extent of alteration. Thin section descriptions also include microtextural information on serpentinization (Fig. F5). The distinction between pseudomorphic, nonpseudomorphic, and transitional serpentinization (see Table T1) provides useful information, as only pseudomorphic textures are primary alteration features, whereas the latter two represent recrystallization phenomena. Microtextural criteria were combined with optical orientation of serpentine fibers (or apparent fibers) to accomplish a tentative identification of chrysotile and lizardite (Table T3).

X-Ray Diffraction

Phase identification in selected samples of whole-rock shipboard powders and metamorphic vein material was aided by XRD analyses using a Philips model PW1729 X-ray diffractometer with $\text{CuK}\alpha$ radiation (Ni filter). Each sample was freeze-dried, crushed, and mounted with random orientation in an aluminum sample holder. Instrument conditions were as follows:

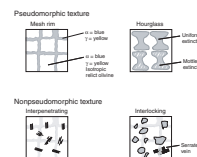
Voltage = 40 kV,
Current = 35 mA,
Goniometer scan (bulk samples) $2^\circ\text{--}70^\circ 2\theta$,
Step size = $0.02^\circ 2\theta$,
Scan speed = $1.2^\circ 2\theta/\text{min}$, and
Count time = 1 s.

Peak intensities were converted to values appropriate for a fixed slit width. An interactive software package (MacDiff version 4.1.1. PPC) was used on a Macintosh computer to identify the primary minerals (public domain software is available at www.pangaea.de/Software). Identifications were based on multiple peak matches, using the mineral database provided with MacDiff. Relative proportions of serpentine (a distinction between the different polytypes was usually not possible), brucite, zeolites, carbonates, magnetite, calcium silicates, pyroxene, amphibole, chlorite, and clay minerals were estimated using peak intensity ratios. Relative abundances reported in this volume (trace, minor, and major components) are useful for general characterization but are not precise.

STRUCTURAL GEOLOGY

Conventions for structural studies established during previous “hard rock” drilling legs (e.g., Legs 118, 131, 140, 147, 153, 176, and 179) were generally followed during Leg 209. However, several minor changes in nomenclature and procedure were adopted. These changes are described below. Where procedures followed directly from previous legs, references to the appropriate *Initial Reports* “Explanatory Notes” chapter are given.

F5. Serpentine microtextures, p. 47.



T3. Serpentine identification key, p. 61.

Overview of Macroscopic Core Description

All descriptions and structural measurements during Leg 209 were made on the archive halves of the cores. Following procedures described in the Leg 153 *Initial Reports* volume (Shipboard Scientific Party, 1995), data were entered into a VCD form (Fig. F2) used in conjunction with four spreadsheet logs. The structural sketches are intended to illustrate the most representative structures and crosscutting relationships in a core section; in addition, a brief general description of the structures is printed on the VCD form (see the “**Supplementary Materials**” contents list). Paper copies of spreadsheet forms were used for recording specific structures and measurements during core description. Separate spreadsheets were used to record data on

1. Alteration veins;
2. Breccias, faults, joints, drilling-induced fractures, serpentinization fabrics, and cataclastic fabrics;
3. Crystal-plastic fabrics and sense of shear indicators; and
4. Magmatic fabrics, magmatic veins, compositional layering, and igneous contacts.

The description and orientation of all features were recorded using curated depth so that “structural intervals” could be correlated with other lithologic intervals. The spreadsheets were organized to record seven separate types of measurements using the deformation intensity scales summarized in Figure F6. The structural geologists worked together during the same shift to minimize measurement inconsistencies. Each member of the team was responsible for making a specific set of observations throughout the entire core (e.g., characterization of crystal-plastic fabric intensity).

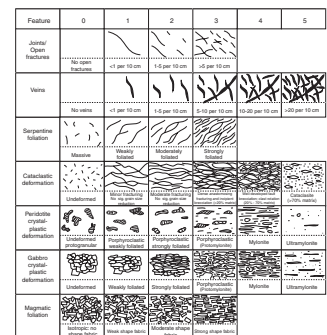
Nomenclature

To maintain consistency of core descriptions, we used feature identifiers for structures similar to those outlined in Shipboard Scientific Party (1995). Modifications to this scheme are shown in the comments checklist (Table T4) and include designation of breccia type (hydrothermal [Bh], cataclastic [Bc], or magmatic [Bm]). Where brittle fabrics overprint crystal-plastic fabrics or deformation was “semibrittle,” a note was made in the comments section and documented in the cataclastic fabrics (brittle structures) spreadsheet (see the “**Supplementary Materials**” contents list).

Structural Measurements

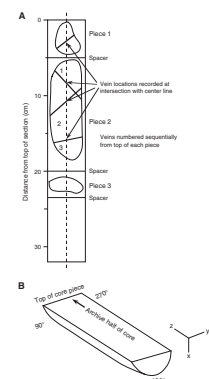
Structural features were recorded relative to core section depths in centimeters from the top of the core section. Depth was defined as the point where the structure intersects the center of the cut face of the archive half of the core (Fig. F7) or, if the feature does not appear in the center of the core, the depth of the centroid of the feature in the archive half of the core. Crosscutting relationships were described in intervals delimited by top and bottom depth. Apparent fault separations of planar markers along faults were recorded as they appeared on the cut face of the archive half of the core and the end of broken pieces. Separations seen on the vertical core cut face were treated as dip-slip components of movement and labeled either normal or reverse for

F6. Structural identification intensity scales, p. 48.



T4. Structural identifier checklist, p. 62.

F7. Core reference frame, p. 49.



faults inclined $<90^\circ$; their displacement in millimeters was also recorded. Shear sense indicators were also marked on the core barrel sheets. For vertical fractures, vertical separations were recorded as up or down (e.g., up to the west or down to the east). Separations of features visible on the upper and lower surfaces of core pieces (horizontal planes) were treated as strike-slip components of movement and either marked sinistral or dextral. Separations were measured between displaced planar markers, parallel to the trace of the fault. Slickenside and/or slickenfiber orientation trend and plunge measurements or the trend and plunge direction of the slip line between offset linear markers were incorporated wherever possible to determine dip-slip, oblique-slip, or strike-slip components. Spinel lineations were determined on acid-leached oriented cubes sawn from representative core sections in the working half. The structures were oriented with respect to the core reference frame; the convention that was used for the core reference frame is explained in Shipboard Scientific Party (1995) (Fig. F7) and shown at the top of the comments box in the structural data spreadsheets (see “[Supplementary Materials](#)” contents list).

Planar structures were oriented using the techniques outlined during Leg 176 (Shipboard Scientific Party, 1999a). Apparent dips in the cut plane of the archive core were recorded as two-digit numbers (between 00° and 90°) with apparent-dip azimuth either as 090° or 270° (Fig. F7). A second apparent dip was recorded in a different orientation with different apparent-dip azimuths (usually either 000° or 180°). The two apparent dips and their azimuths were used to calculate the true dip and strike direction with respect to the core reference frame. These calculations were performed using a macro routine within each Excel spreadsheet.

The true dip and strike directions of the samples were reoriented using available paleomagnetic declinations to rotate the measurements to a common alignment. The orientation of this common alignment was chosen to have an azimuth of zero, but this alignment does not necessarily correspond to true north because of the effects of tectonic rotation on the orientation of the magnetic declination direction. The data were plotted on lower-hemisphere stereographic projections using the shareware of R. Allmendinger (www.geo.cornell.edu/geology/faculty/RWA/RWA.html) and the careware of D. Mainprice (www.isteam.univ-montp2.fr/TECTONOPHY/petrophysics/software/petrophysics_software.html).

Fabric Intensities

A semiquantitative scale of deformation and magmatic and alteration fabric intensities was used by the shipboard structural geologists during core description. This scale, shown in Figure F6, was modified from the deformation scales used during Leg 147 (Shipboard Scientific Party, 1993, table 2) and the fabric intensity scales used during Legs 153 and 176 (Shipboard Scientific Party, 1995, fig. 13; 1999a, table T2) and conforms to the deformation texture scales used by Cannat et al. (1991) and Dick et al. (1991). Wherever possible we have assigned specific values to intensity estimates (e.g., vein spacing or matrix percentage in a cataclastic zone) to maintain consistency throughout the core. However, for some categories this proved difficult (e.g., the intensity of any crystal-plastic fabric), in which cases we used qualitative estimates of intensity based on hand-specimen and thin section observations. We documented six distinct types of fabric intensity measurements (Fig. F6):

1. **Magmatic:** presence and intensity of any shape-preferred orientation of magmatic phases. Four levels, from no shape-preferred orientation (0) to a strong shape-preferred orientation (3), were used. Where no or only a very weak magmatic fabric was present in gabbroic rocks (predating any other structure), the Structural column was left blank. Plagioclase and pyroxene “impregnation structures” in peridotites were described in the same manner.
2. **Crystal plastic:** six levels of deformation intensity were used, ranging from a lack of any crystal-plastic fabric, through three stages of foliation and porphyroclast development, to mylonitic and ultramylonitic fabrics. The textural criterion used for gabbroic rocks on which this was based was modified slightly for peridotites as described below.
3. **Cataclastic:** six levels of deformation intensity were used with fabrics categorized depending on the percentage of matrix present within each cataclastic zone. Thin section descriptions, wherever possible, significantly aid this categorization.
4. **Joints (fractures without shear displacements):** four levels of joint density were used, depending on the average frequency of joints across a 10-cm depth interval along the long axis of the core. Joints were distinguished from faults (cataclastic features) by the lack of any identifiable offset.
5. **Veins (filled fractures):** six levels of vein density were used, depending on the average frequency of veins across a 10-cm depth interval along the long axis of the core. Alteration veins are those which contain metamorphic phases. In some cases these may have originally been igneous, but no primary phases or their characteristic pseudomorphs were recognized. Magmatic veins are compositionally distinct mineral segregations that may be concordant or discordant.
6. **Serpentine foliation:** formation of strong planar fabrics may occur during serpentinization by development of closely spaced subparallel veins termed ribbon texture (O’Hanley, 1996). The texture is characterized by anastomosing, often cross-fiber, replacement serpentine veins. In general, the veins wrap around relict or pseudomorphed pyroxene grains with little evidence of shear offset. These create a strongly foliated serpentinite that is actually a variant of hourglass serpentine texture and largely represents in situ replacement of the primary olivine (O’Hanley, 1996). This texture may parallel preexisting crystal-plastic foliation, and its intensity may reflect stress state or the presence of a preexisting fabric in the rock. The strength of serpentine foliation is rated on a scale from 0 (massive, no foliation) to 3 (strongly foliated).

Occasionally it proved difficult to differentiate between crystal-plastic and cataclastic deformation in relatively high strain shear zones based on hand-specimen observations only. For this reason, as during Leg 147, we tried to classify both of these deformation styles using parallel scales where a certain intensity of cataclastic is a direct equivalent to the same intensity of crystal-plastic deformation. Some sections of the core contained small subhorizontal microfractures commonly related to unloading accompanying drilling. To avoid unnecessary measurements of these drilling-induced features, a column was added to the cataclastic fabric spreadsheet to indicate the density of these features using the same scale as for joints.

Abyssal peridotites represent a special problem for grading crystal-plastic deformation, as they have usually been emplaced from the Earth's deep interior by high-temperature crystal-plastic creep processes and, hence, lack a primary igneous texture. They generally have either protogranular or porphyroclastic textures when unmodified by relatively shallow deformation processes associated with unroofing and exposure to the seafloor. *Protogranular* textures are generally the earliest fabric and are characterized by smoothly curved grain boundaries with complex cusps and lobes (Fig. F6). However, alteration has generally entirely obscured olivine grain size and shape in hand specimen in abyssal peridotites, so the visual core description is almost entirely based on pyroxene and spinel textures. Rocks with a purely protogranular texture are graded 0, as this is the earliest formed texture and may or may not have a preferred crystallographic mineral fabric or a shape fabric. *Porphyroclastic* textures are generally superimposed on protogranular, and frequently elements of both are present. In this case we used the name of the predominant texture, but the intensity grade 0.5 indicates that elements of both textures are prominent. Rocks with porphyroclastic texture are graded 1 if there is only a weak or no pyroxene shape fabric developed. When pyroxenes exhibit a significant shape fabric, then the sample is graded a 2 under the crystal-plastic field, noting that at this grade only a few protogranular textural elements are present. These samples are still referred to as porphyroclastic. When the shape fabric starts to become strong and a foliation develops, accompanied by significant grain size reduction (protogranular abyssal peridotites generally have a pyroxene grain size of around 3–6 mm), the texture is referred to as *protomylonite* and graded 3 under crystal-plastic deformation. At this grade there are generally no protogranular textural elements left. When the peridotite has significant grain size reduction and consists of a fine-grained mass of olivine with embedded pyroxene porphyroclasts and a prominent foliation, the rock is graded 4 and listed as a *mylonite*. If there is no visible foliation due to extreme grain-size reduction, the rock is listed as an *ultramylonite* and graded 5. This deformation scale closely parallels that used for gabbro here and during previous legs and represents very similar or the same intensities of deformation at each grade.

Thin Section Descriptions

Thin sections were examined to characterize the microstructural aspects of important mesoscopic structures in the core. Classes of information that were obtained include deformation mechanisms on a mineral-by-mineral basis, kinematic indicators, crystallographic (where obvious) and shape fabrics, qualitative estimates of the degree of crystallographic preferred orientation along local principal finite strain axes, syn- and postkinematic alteration, and the relative timing of microstructures. The orientation of thin sections relative to the deformation fabrics and core axes is noted in the comments section of the spreadsheet. Thin sections were oriented, where possible, with respect to the core axis and in the core reference frame described in "[Structural Measurements](#)," p. 10. Selected samples were cut perpendicular to the foliation and parallel to any lineation to examine kinematic indicators and the shape-preferred orientation of minerals. We adopted and modified the thin section description form used by the structural geologists during Leg 140 (Shipboard Scientific Party, 1992) to enter the micro-

structural information into the spreadsheet database (see the “[Supplementary Material](#)” contents list).

A large variety of microstructures occur in gabbros (see “Igneous Petrology,” p. 12, and “Structural Geology,” p. 54, in Shipboard Scientific Party, 1999b). For the purposes of entering data into spreadsheets here, a number of textural types characterized by specific microstructural styles were used based on the Leg 176 and 153 systems, modified slightly to accommodate description of peridotites. These are summarized in Table T5. It is possible that superposition of different microstructures or deformation mechanisms may occur during cooling. Thus, the physical state of the material during fabric development may span the transition from hypersolidus to subsolidus. Igneous fabrics defined entirely by minerals with no crystal-plastic deformation microstructures are termed magmatic. Where local crystal-plastic fabrics are produced in the presence of melt (e.g., Hirth and Kohlstedt, 1995; Bouchez et al., 1992; Means and Park, 1994; Nicolas and Ildefonse, 1996), we term the physical state “crystal plastic ± melt.” Where fabric development is produced entirely by dislocation creep, we use the term “crystal plastic” to define the physical state of the rock.

T5. Gabbro microstructure, p. 64.

GEOCHEMISTRY

During Leg 209, we performed chemical analyses of samples selected by the shipboard scientific party using inductively coupled plasma-atomic emission spectrometry (ICP-AES) and gas chromatography. Various lithologies, including peridotite, serpentinite, and gabbro, were analyzed for major oxide and selected trace element compositions. Sampling and analytical procedures were adapted from those developed during Legs 147, 153, 176, 187, 197, and 203, and the overall strategy is described in ODP *Technical Note 29* by Murray et al. (2000). The shipboard analytical facilities are described in the Leg 147 and 187 *Initial Reports* volumes (Shipboard Scientific Party, 1993 and 2001, respectively). The ICP-AES was first used during Leg 187, and additional details are given in the Leg 197 *Initial Reports* volume (Shipboard Scientific Party, 2002).

ICP-AES Analyses of Major and Trace Elements

Sample Preparation

Selected representative samples were first cut with a diamond-impregnated saw blade and wet-ground on a diamond abrasive wheel to remove surface contamination. Samples were then washed in an ultrasonic bath containing methanol for ~10 min, followed by three consecutive ~10-min washes in an ultrasonic bath containing nanopure deionized water. They were then dried for ~12 hr in an oven at 110°C. The cleaned whole-rock samples (~10 cm³ in size) were reduced to fragments <1 cm in diameter by crushing them between two disks of Delrin plastic in a hydraulic press, followed by grinding for ~5 min in a Spex 8510 shatterbox with a tungsten carbide barrel. Approximately 1 g of sample powder was weighed on a Scientech balance and ignited at 1025°C for 4 hr to determine weight loss on ignition (LOI).

Aliquots of 100 ± 2 mg of the ignited whole-rock powders were mixed with 400 ± 0.4 mg of lithium metaborate (LiBO₂) flux that had been preweighed on shore. All samples and standards were weighed on

the Cahn Electrobalance under computer control. Weighing errors are conservatively estimated to be ± 0.01 mg.

Mixtures of flux and rock powders were fused in Pt-Au crucibles at 1050°C for 10–12 min in a Bead Sampler NT-2100. Ten microliters of 0.172-mM aqueous lithium bromide (LiBr) solution was added to the mixture before fusion as an antiwetting agent to prevent the cooled bead from sticking to the crucible. Cooled beads were transferred to 125-mL polypropylene bottles and dissolved in 50 mL of 2.3-M nitric acid (HNO₃) by shaking with a Burrell Wrist Action bottle shaker for 1 hr. After digestion of the glass bead, all of the solution was filtered to 0.45 μ m into a clean 60-mL wide-mouth polypropylene bottle. Next, 2.5 mL of this solution was transferred to a plastic vial and diluted with 17.5 mL of 2.3-M HNO₃ to bring the total volume to 20 mL. This solution-to-sample dilution, used for major and trace elements, is 4000. Dilutions were made using a Brinkman dispensette (0.25 mL).

Analysis

Major (Si, Ti, Al, Fe, Mn, Mg, Ca, Na, P, and K) and trace (Sr, V, Cr, Co, Ni, Cu, Sc, Y, Zr, and Ba) element concentrations of powder samples were determined with the JY2000 Ultracore ICP-AES. The JY2000 sequentially measures characteristic emission intensities (with wavelengths between ~100 and 800 nm). P was systematically below detection limits in peridotites and gabbroic rocks in Site 1268 samples and in ultramafic standards (JP-1, DTS-1, and ROA-3). Therefore, we did not analyze this element at the other sites. We routinely ran two element menus, major elements (Si, Fe, Mg, Mn, Al, Ca, and Na) and trace elements (Ti, K, and trace elements listed above). Standard rock powders, calibration and drift solutions, and chemical blanks were included with the unknowns for each sample run. Murray et al. (2000) developed protocols for dissolution and ICP-AES analysis of rock powders. The hard rock analytical procedure was refined during a previous expedition (Leg 197; Shipboard Scientific Party, 2002). The elements analyzed, emission lines used, limits of detection, and specific analytical conditions during Leg 209 are provided in Table T6.

The JY2000 plasma was ignited 30 min before each run to allow the instrument to warm up and stabilize. After the warm-up period, a zero-order search was performed to check the mechanical zero of the diffraction grating. After the zero-order search, the mechanical step positions of emission lines were tuned by automatically searching with a 0.002-nm window across each emission peak using BHVO-2 standard prepared in 2.3-M HNO₃. During the initial setup, an emission profile was collected for each peak, using BHVO-2, to determine peak-to-background intensities and to set the locations of background points for each element. The JY2000 software uses these background locations to calculate the net intensity for each emission line. The photomultiplier voltage was optimized by automatically adjusting the gain for each element using the standard (either BHVO-2 or DTS-1) with the highest concentration for that element. Before each run, a profile of BHVO-2 was collected to assess the performance of the instrument from day to day. A typical analytical session for 12 samples lasted ~9 hr, depending on the number of replicate analyses.

All ICP-AES data presented in the site chapters were acquired using the Gaussian analytical mode (mode 2) of the Windows version 5.01 JY2000 software. This mode was used to fit a Gaussian curve to five points, each measured for 1 s, across a peak. The fit was then integrated

T6. ICP-AES analytical conditions, p. 65.

to determine the area under the curve. The analysis time required in this mode is about three times that needed to simply measure a single peak intensity, but it leads to considerable improvement in analytical precision (Leg 187; Shipboard Scientific Party, 2001). Each unknown sample was run at least twice, nonsequentially, in all sample runs. We used the concentric nebulizer for the JY2000 because it delivers a finer aerosol to the plasma and results in a more stable signal (Leg 187; Shipboard Scientific Party, 2001). However, use of this nebulizer requires filtering the solutions and somewhat greater sample dilution factors to reduce clogging.

ICP-AES runs included the following:

1. A set of three certified rock standards (BIR-1, JP-1, and DTS-1) (Table T7) at the beginning, middle, and end of the analytical session;
2. Up to 12 unknown samples;
3. A drift-correcting sample (the BHVO-2 standard) analyzed every fifth sample position; and
4. Blank solutions at the beginning and end of each session.

A 2.3-M HNO₃ wash solution was run for a minimum of 90 s between each of the samples and standards. The following is an example of a typical run menu for 12 samples, requiring ~9 hr of instrument time: drift, blank, DTS-1, BIR-1, drift, sample 1, sample 2, sample 3, ROA-3, drift, sample 4, sample 5, sample 6, BIR-1 (run as an unknown), drift, sample 7, sample 8, sample 9, ROA-3, drift, sample 10, sample 11, sample 12, blank, drift, DTS-1, BIR-1, drift. During the earlier parts of an analytical session the drift solution is run more frequently, after which it is run at regularly spaced intervals to simplify data reduction. Analytical sessions usually included two analyses of ROA-3, a pyroxenite from the Ronda ultramafic massif previously prepared and analyzed on shore. Use of this secondary standard and BIR-1, run as unknowns, provides a means to realistically assess both analytical accuracy and external precision.

Data Reduction

Following each analytical session, the raw intensities were transferred to a data file and data reduction was completed using a spreadsheet to ensure proper control over standardization and drift correction. Once transferred, intensities for all samples were corrected for the procedural blank. A drift correction was then applied to each element by linear interpolation between the drift-monitoring solutions run before and after a particular batch of samples. The interpolation factor for each sample is based on the time of the analysis. Following blank subtraction and drift correction, element concentrations for each sample were calculated from the average intensity per unit concentration for the standards JP-1, BHVO-2, BIR-1 (two of three runs), and DTS-1. The blank was also included in the regression with both its intensity and concentration set to zero. The regression technique gave good correlation coefficients (>0.99 for all elements except Co [>0.96] and Ba [>0.97]) for most oxides and trace elements. It also revealed either important discrepancies and/or problems with sample preparation (e.g., in the case of Cu, which is not reported in the site chapters).

Estimates of accuracy and precision for major and trace element analyses are based on replicate analyses of ROA-3 and BIR-1, the results of which are presented in Table T7. In general, run-to-run relative preci-

T7. ICP-AES accuracy and precision, p. 66.

sion by ICP-AES was better than 2% for the major elements. Run-to-run relative precision for minor and trace elements was generally <5% except when elements were near the detection limit of the instrument (see Table T6 for instrument detection limits).

Gas Chromatography

To more fully investigate LOI for each sample, gas chromatographic separation of sample volatiles was carried out using a Carlo Erba NA 1500 CHS analyzer, in which the respective gaseous oxides of C, H, and S are quantitatively determined by a thermal conductivity detector. The sample introduction system has a vertically mounted quartz tube containing small pellets of reduced Cu, separated by a small amount of quartz wool from tungstic anhydride, which acts as a catalyst. Samples are dropped into the tube in tin boats and heated at 1010°C in the presence of oxygen for ~75 s. During this time, nitrogen, hydrogen, carbon, and sulfur released from the sample are oxidized and swept into the gas chromatograph (GC) using helium carrier gas. The sulfur from sulfide minerals is oxidized to SO₂, and SO₂ is released from any sulfate minerals present in the sample. Aliquots of sulfanilamide (C₆H₇N₂O₂S) weighing between ~1 and 3 mg were used for primary calibration of the instrument. A single sample analysis requires ~12 min. During this time, signal intensity at the detector was continuously recorded, and N, C, H, and S separated by the GC were measured sequentially at ~60, 120, 320, and 465 s. Following blank subtraction, concentrations for each sample were calculated from the integrated peak areas of the respective gases relative to those for the standard using a linear regression. The blank was included in the regression with both its intensity and concentration set to zero. The regression technique usually gave good correlation coefficients (>0.99).

Sample analyses were performed on rock powders dried at 110°C for 12 hr. For Sites 1268 through 1271, sample sizes were typically 30–40 mg. This relatively large amount of sample was initially chosen in an attempt to optimize the analysis of CO₂ in serpentinized peridotite. However, 30 mg of serpentinized peridotite releases about an order of magnitude more H₂O than the standard calibration using sulfanilamide. After Site 1271, it became very evident that analysis of the larger (30–40 mg) samples leads to a bias of 10%–20% in measured water content, so the sample size was reduced to 5–10 mg to optimize the analysis of H₂O concentration. This bias estimate is based on comparison of measured and accepted values for three secondary standard rocks routinely analyzed as unknowns during each analytical session. The three secondary standards are a shipboard diabase standard BAS140 (Sparks and Zuleger, 1995; Bach et al., 1996), a peridotite standard JP-1, and an altered basalt from Leg 147 (Sample 147-895D-10W; Puchelt et al., 1996). Typical analytical sessions included multiple analyses of each of these standard rocks, to provide a test of the accuracy and reproducibility of the methods. Results of the GC analyses for BAS140, Sample 147-895D-10W, and JP-1 are presented in Table T8. Detection limits, calculated as three times the standard deviation of all the blank analyses, are CO₂ = 0.04 wt%, H₂O = 0.15 wt%, and S = 350 ppm. In comparing the GC volatile analyses to the LOI results, it is also important to bear in mind that conversion of Fe²⁺ to Fe³⁺ during ignition may produce a gain in weight that is 11.1% of the percentage of ferrous Fe contained in the sample. This can lead to LOI results that are less than the volatile concentra-

T8. Gas analyses accuracy and precision, p. 70.

tions determined by GC. Because of a technical problem, S was not analyzed in most of the Site 1270 rocks.

Complete sample analyses are available in data tables (see the “[Supplementary Materials](#)” contents list) and in the “Geochemistry” sections in each site chapter.

PHYSICAL PROPERTIES

Shipboard measurements of physical properties are used to characterize lithologic units and alteration processes, for correlating cored material with downhole logging data, and for interpreting seismic reflection profiles.

After recovery, the cores were allowed to come to room temperature (22°–23°C), then thermal conductivity, natural gamma radiation (NGR), and magnetic susceptibility were measured in a series of nondestructive tests. Additional measurements of *P*-wave velocity, bulk and grain density, porosity, and water content were made on right circular cylinders, cubes, and chips cut from the split core. Most of these samples were also used for paleomagnetic measurements.

Nondestructive Tests

Four sets of measurements (magnetic susceptibility, gamma ray attenuation [GRA] density, *P*-wave velocity, and NGR) can be made in sequence on whole-core sections on the MST. MST data are sampled at discrete intervals, with sampling intervals and count times chosen to optimize the resolution of the data in the time available to run each core section through the device. During Leg 209, no advanced piston corer or extended core barrel sediment cores were taken; consequently, only magnetic susceptibility and NGR measurements were made on the rotary core barrel (RCB) cores.

Magnetic Susceptibility

The MST includes a Bartington susceptibility meter (model MS2C) that has an 8-cm loop and operates at 0.565 kHz with a field intensity of 80 A/m. Volume susceptibility, *k*, is a dimensionless measure of the degree to which material can be magnetized in an external magnetic field,

$$k = M/H,$$

where *M* is the magnetization induced in the material by an external field of strength *H*. Magnetic susceptibility is sensitive to variations of the type and concentration of magnetic grains in the rocks and is thus an indicator of compositional variations. During Leg 209, we sampled RCB cores at 2.5-cm intervals. On the Bartington MS2C sensor, all readings >0.1 SI are clipped, so that the most significant digit of the susceptibility value is not recorded. The data from the MST system are given in 10⁻⁵ SI. They represent the volume susceptibility for a core with a diameter of 6.6 cm. The diameter of the Leg 209 cores was always smaller (~5.5–6.0 cm); therefore, the true susceptibility is underestimated.

GRA Density

The GRA densitometer was not used during Leg 209.

P-Wave Velocity

The P-wave logger was not used during Leg 209.

Natural Gamma Radiation

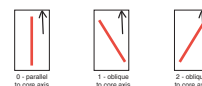
Natural gamma radiation was logged on the MST using a 30-s counting period at 10-cm intervals.

Thermal Conductivity

Thermal conductivity is measured by transient heating of the sample with a known heating power generated from a source with assumed infinite length, finite radius, and assumed infinite thermal conductivity (7-cm-long needle) and measuring the temperature change with time using the TK04 system described by Blum (1997). The variation of temperature with radial distance from the source depends on the thermal conductivity of the sample, which is assumed to be homogeneous. The needle probe method is used in half-space mode (Vacquier, 1985) to measure thermal conductivity in pieces of the split core taken from the archive half. Samples were taken at irregularly spaced intervals, depending on the availability of pieces long enough to be measured and on the lithologic variability. Measurements are made at room pressure and temperature; they are not corrected to in situ conditions. The shipboard measurement conditions are not optimal, as the measurement setup is not always in perfect thermal equilibrium because of room temperature changes due to frequently opened doors and circulating people. Each reported thermal conductivity value is an average of four measurements, with the smallest possible standard deviation (<0.03 W/[m·k] in most cases). In the site chapters, Leg 209 data are compared to previous data for gabbros and peridotites from Legs 118 (Robinson, Von Herzon, et al., 1989), 147 (Gillis, Mével, Allan, et al., 1993), 153 (Cannat, Karson, Miller, et al., 1995), and 176 (Dick, Natland, Miller, et al., 1999). However, these (except for Leg 176) were acquired with the Thermcon-85 system, which was replaced on board the *JOIDES Resolution* by the TK04 system in 1996 (Leg 168). The latter probably gives more accurate and consistent results, as the new measurement technique is less user-dependent than the older one (Blum, 1997).

The measurement method used on board the *JOIDES Resolution* (Blum, 1997) assumes the sample is isotropic. However, thermal conductivity is an intrinsic tensor material property that depends on porosity, density, mineral composition, and fabrics. Most known single-crystal thermal diffusivities are anisotropic (e.g., Kobayashi, 1974; Tommasi et al., 2002). Therefore, thermal conductivity is expected to be anisotropic. To evaluate the anisotropy of thermal conductivity in the peridotites and gabbros, we ran, whenever possible, three measurements on the cut face of each sample, one parallel to the core and two at angles of $\sim 35^\circ$ to the core axis (Fig. F8).

F8. Thermal conductivity needle probe orientation, p. 50.



P-Wave Velocity

The PWS3 (Hamilton Frame) was used to measure velocities in discrete samples (minicores and cubes) of the materials recovered during Leg 209. The PWS3 is a modified and updated version of the classic Hamilton Frame velocimeter, in which one transducer is fixed and the other is mounted on a screw. The PWS3 is mounted vertically to measure velocities perpendicular to the core axis by placing the sample on the lower transducer and bringing the upper transducer into direct contact with the upper surface. To improve the coupling (i.e., the impedance match) between the transducer and the sample, water is commonly applied to the top and bottom of the sample and transducer heads. Traveltimes are picked manually or automatically by the threshold method, and the transducer separation is recorded by a digital caliper.

Porosity and Density

The minicores and cubes used for velocity measurements were also used to estimate bulk density, grain density, and porosity from the wet weights and dry weights or volumes of the samples. Volumes were calculated from the dimensions of the samples, measured using either a hand caliper or the PWS3 digital caliper. In the course of our analysis of data from Site 1272, we found that the latter method is subject to a systematic mean error in the length of ~0.5%, which is not enough to affect the PWS3 velocities but leads to a systematic overestimate of sample volume and a corresponding underestimate of bulk density of ~1.5% (~4 kg/m³). Sample mass was determined to a precision of ±0.001 g using two Scientech electronic balances. The balances are equipped with a computer averaging system that compensates for the motion of the ship. The sample mass on one balance is counterbalanced by a known mass on the adjacent balance. The volumes of chips and some minicores were determined using a five-cell Quantachrome helium-displacement pycnometer with a nominal precision of ±0.01 cm³. Measurements were repeated until a standard error <0.02 cm³ was achieved. A standard reference sphere was run sequentially in each of the five operating cells to maintain calibration. The cell volume was recalibrated if the measured volume of the standard was not within 0.02 cm³ of the known volume of the standard. Dry weight and pycnometer volume measurements were made after the samples were oven dried at 105° ± 5°C for 24 hr and allowed to cool in a desiccator. A potential problem with this drying temperature is that, in addition to interstitial water, chemically bound water in some clay minerals can be lost.

Water Content

Water content, as a fraction of total mass or as a ratio of water mass to solid mass, is determined by standard methods of the American Society for Testing and Materials (ASTM) designation (D) 2216 (ASTM, 1989). The total water-saturated mass (M_b) and dry mass (M_d) are measured using the electronic balance as described above, and the difference is the uncorrected water mass. Measured wet and dry masses are corrected for salt assuming a pore water salinity (s) of 0.035 (Boyce, 1976). The water contents expressed as a percentage of the wet mass or the dry mass (W_b and W_s , respectively) are given by

$$W_s (\%) = 100[(M_b - M_d)/(M_d - sM_b)] \text{ and}$$

$$W_b (\%) = 100[(M_b - M_d)/(1-s)M_b],$$

where M_b = the mass of the saturated sample.

Bulk Density

Bulk density (ρ_b) is the density of the saturated sample,

$$\rho_b = M_b/V_b,$$

where V_b = the total sample volume, which is estimated from the dimensions of the sample or from the volume of the dry sample (V_d) and the volume of the pore fluid (V_{pw}) (see below):

$$V_b = V_d + V_{pw}.$$

Grain Density

Grain density (ρ_g) is determined from the dry mass and dry volume measurements. Both mass and volume must be corrected for the salt content of the pore fluid,

$$\rho_g = (M_d - M_{salt})/(V_d - M_{salt}/\rho_{salt}),$$

where M_d = the dry mass of the sample (in grams) and ρ_{salt} = the density of salt (2.257 g/cm³), where

$$M_{salt} = s(M_b - M_d)/(1-s)$$

is the mass of salt in the pore fluid and M_{pw} is the salt-corrected mass of the seawater

$$M_{pw} = (M_b - M_d)/(1-s).$$

The volume of pore water is

$$V_{pw} = (M_b - M_d)/(1-s)\rho_{pw},$$

where ρ_{pw} = the density of the pore fluid, which is assumed to be seawater.

Alternatively, the grain density is calculated from the wet and dry masses (M_b and M_d) and the sample volume (V_b) is calculated from the measured dimensions of a minicore or cube sample:

$$\rho_g = (M_d - M_{salt})/[(1-s)\rho_{pw}/(M_b - M_d)].$$

Porosity

Porosity (ϕ) is the ratio of pore water volume to total volume and can be calculated from fluid density, grain density, and bulk density of the material:

$$\phi = 100[(\rho_g - \rho_b)/(\rho_g - \rho_w)],$$

where ρ_g = the grain density and ρ_b = the bulk density.

Dry Density

The dry density (ρ_d) is the ratio of the dry mass (M_d) to the total volume (V_b). The dry density is calculated from the corrected water content (W_d) and porosity (ϕ):

$$\rho_d = (\phi/W_d)\rho_w.$$

PALEOMAGNETISM

Paleomagnetic and rock magnetic investigations during Leg 209 were designed primarily to

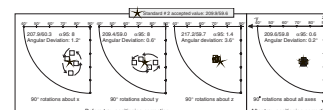
1. Evaluate possible tectonic rotations,
2. Determine the characteristic remanence directions to allow possible reorientation of structural features in the cores,
3. Assess the orientation and significance of magnetic fabrics, and
4. Evaluate the suitability of the sampled materials as a source for marine magnetic anomalies.

Paleomagnetic measurements were performed on discrete minicore and cube samples and, where practical, on continuous pieces of the archive halves. The azimuths of core samples recovered by rotary drilling are not constrained. All magnetic data are therefore reported relative to the following core coordinates: +x (north) is into the face of the working half of the core, +y (east) points toward the right side of the face of the working half, and +z is down (Fig. F9).

The remanence of archive halves was measured using a pass-through 2G Enterprises direct-current Superconducting Quantum Interference Device (DC-SQUID) rock magnetometer (model 760R). The magnetometer is equipped with an in-line alternating-field (AF) demagnetizer (2G model 2G600) where samples can be demagnetized to peak fields of 80 mT. Both the magnetometer and AF demagnetizer are interfaced with a computer and are controlled by the 2G Long Core software (Core Logic, version Leg207.3). The maximum intensities that could be measured while still maintaining an accurate count of flux quanta (i.e., where the number of flux counts returns to zero after the measurement) depends on the velocity of measurements. Archive halves were typically measured at a tray velocity of 1–5 cm/s to prevent the loss of flux counts. Because the response functions of the SQUID sensors have a full width of ~10 cm at half height, data within 5 cm of piece boundaries or voids are significantly affected by edge effects. The current version of the Core Logic software allows bypassing measurements in these intervals. We did not perform measurements within 4 cm of a piece end. Although this approach means that no data are collected for pieces smaller than 8 cm or near piece ends, the time savings allows more detailed measurement or more demagnetization steps elsewhere. Archive halves were typically measured at an interval of 2 cm for natural remanent magnetization and after 10- and 20-mT demagnetization.

A standard 2.5-cm-diameter minicore sample or ~9-cm³ cube was generally taken from each 4.5-m cored interval for shipboard study. These discrete samples were chosen to be representative of the lithology and alteration mineralogy, and an effort was made to utilize samples for which geochemical and physical properties were also measured. The remanence of discrete samples was measured primarily using the 2G

F9. Paleomagnetic orientation convention, p. 51.



SQUID magnetometer, with only a small number of samples measured using the Molspin spinner magnetometer (using PMagic software). The shipboard 2G magnetometer is normally set up to measure as many as seven discrete samples, which are separated by 20 cm on a sample tray 150 cm long. Because remanent intensities of the Leg 209 samples may vary by several orders of magnitude, all discrete samples were spaced 35 cm apart to effectively eliminate any contamination of one measurement from the signal of a neighboring sample.

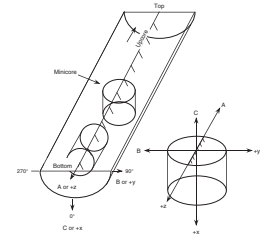
The calibration of the 2G magnetometer for discrete sample measurements was verified by measuring six standards that were the subject of an interlaboratory cross-calibration experiment (L. Tauxe, pers. comm., 2001). The intensities of these standards measured with the shipboard magnetometer agreed well with the accepted values (on average, the shipboard results are 1% higher). As expected from the uncertainties in positioning samples with respect to the magnetometer/SQUID axes, the remanence directions for the standards showed significant deviations (up to 9°) from the accepted values when measurements were made in one single position. When measurements were averaged over 10 different positions, the standards showed average deviations of $\sim 2^\circ$ (Table T9). However, the scatter of directions was not uniform, suggesting that a systematic bias resulted from misalignment between the tray and SQUID axes (Fig. F10). The dispersion of the remanence directions was high when samples were rotated about the magnetometer x- or y-axis. When samples were rotated about the z-axis, the scatter of directions decreased but the angular deviation with respect to the accepted standard values increased. This can be explained as the result of an offset in the x- and y- tray axes with respect to the magnetometer/SQUID axes. A counterclockwise rotation of $\sim 7^\circ$ about the z-axis was applied to the sample holder in order to correct its positioning with respect to the sensors. After this repositioning, measurements over the 10 different positions yielded average directions with an angular deviation $< 1^\circ$ (Table T10). Furthermore, single measurements yielded directions within 2° of the accepted value, independent of the orientation of the sample with respect to the magnetometer axes. In order to provide the most robust directional data, all discrete samples were measured in three positions (such that the magnetization component parallel to each of the sample coordinate axes was measured once with each SQUID sensor) and the data averaged.

Most discrete samples were subjected to stepwise AF demagnetization using a DTech (model D-2000) AF demagnetizer capable of peak fields up to 200 mT. A small number of samples were also thermally demagnetized by the Schonstedt Thermal Specimen Demagnetizer (model TSD-1). Sufficient stepwise AF or thermal demagnetizations were performed to isolate characteristic remanent magnetization components and to quantify magnetic overprints. Characteristic directions were fit using principal component analysis (Kirschvink, 1980).

In addition to standard paleomagnetic measurements, the anisotropy of magnetic susceptibility was determined for most discrete samples using the Kappabridge KLY-2 (Geofyzika Brno) and a 15-position measuring scheme. Unfortunately, the computer interface for the Kappabridge was not functional. The 15 measurements were therefore manually recorded, and the susceptibility tensor and associated eigenvectors and eigenvalues were calculated off-line following the method of Hext (1963). All bulk susceptibility values reported for discrete samples are from the Kappabridge and have been corrected for the true cylindrical or cubic sample volume. For a small number of samples, the anisotropy

T9. Magnetic data for discrete sample standards, p. 71.

F10. Reduction of scatter after tray repositioning, p. 52.



T10. Standard data after tray repositioning, p. 72.

of ARM was also determined. For each of the sample axial directions (i.e., +x, +y, +z and -x, -y, -z), the remanence after a baseline AF demagnetization step (parallel to the subsequent ARM direction) was measured and subtracted from the axial ARM. The remanence anisotropy tensor was then calculated in a manner analogous to that used for the susceptibility tensor.

Whole-core magnetic susceptibility (κ) was measured at 2.5-cm intervals on all sections using the Bartington Instruments susceptibility meter (model MS1: 80-mm loop, 4.7 kHz, SI units) mounted on the multisensor track. Susceptibility measurements were made on the whole core following the establishment of the final curated positions and placement of spacers and are therefore directly comparable with the pass-through measurements of the archive halves.

MICROBIOLOGY

The primary microbiology objective for Leg 209 was to determine the diversity and potential metabolic pathways of microbes in peridotites. To do this, peridotites were collected from the cores for cultivation experiments, onshore characterization of deoxyribonucleic acid (DNA) within the rocks, and examination of extant and fossil microbial activity by various microscope techniques.

Interpretation of results is complicated by the possibility of contamination of samples with microbes from the seawater (surface: used as drilling fluid, and bottom), the ship and drilling equipment, and from postcollection processing of samples. To determine the extent of microbial contamination introduced during drilling, surface and bottom seawater were sampled to characterize DNA and downhole tracer tests were conducted. Postcollection contamination was minimized by using an established sample handling protocol.

Igneous Rocks

Sampling

Whole-round core samples were removed from the split core liner in the core splitting room. The cores were handled with latex gloves washed with 70% ethanol. Drilling-induced contamination of the outer surface was minimized by quickly flaming the outer surface with a propane torch. After the sterilization, the samples were placed in nitrogen-flushed plastic bags (Zip-Lock) and taken immediately to the anaerobic chamber in the microbiology laboratory. Samples for enrichment cultures were kept moist with sterile artificial seawater and cool with ice.

Pieces of core, kept moist with 1 mL of artificial seawater, were broken with a hydraulic rock splitter and then gently crushed into smaller grains in a sterile steel mortar. Additional pieces of core were used whole as described below.

Enrichment Cultures

Fourteen types of bacterial culture media—all microaerophilic—were used to cultivate viable microbial populations from the rock samples. The media were based on the composition of seawater, and the cultures were contained in airtight Balch tubes. Nitrate, Mn(IV), Fe(III), S(IV), dimethylsulfoxide, and fumarate were added as electron acceptors, and

the solutions were buffered to pH 7.5 and 9.5. Approximately 1 g of crushed rock was added to 20 mL of each type of culture medium. Additionally, each culture tube contained ~5 g of sterile olivine with Fe(II) as the electron donor. Mercuric chloride was added to one of each media type to inhibit all biological reactions within the tube. Uninoculated negative controls were incubated with each medium as well. These controls allow for differentiation of abiotic and biotic reactions in the growth media. Samples were incubated at 4° and 15°C in nitrogen-filled containers. Growth is confirmed by the accumulation of metabolic products and microbial cells.

Hydrothermal clay cultures were set up with the 14 enriched media listed above. Approximately 1 g of clay from the core interior was added to 15 mL of each type of culture medium. Similarly, mercuric chloride was added to one of each media type to inhibit all biological reactions within the tube. Samples were incubated at 4° and 15°C. Growth is confirmed by the accumulation of metabolic products and microbial cells.

A small fragment of core (>1 g) from the interior of the larger microbiology core segment was placed in the bottom of a 50-mL tube and overlain with 25 mL of R2A medium that had been precooled to ~48°C. Additionally, another fragment of core was inoculated into marine broth supplemented with 5% tryptic soy broth. The tubes were capped and incubated at room temperature in the dark for the duration of the leg. Sample tubes were monitored daily for growth. If growth occurred, broth media was inoculated by sterile loop, incubated at room temperature for 48 hr, and archived in glycerol at -70°C. Molecular techniques will be utilized during shore-based analysis of isolates and/or core fragments.

DNA Extraction

Whole-rock pieces split from the cores adjacent to the pieces used for culture experiments were preserved for shore-based DNA extraction. Rocks were frozen at -80°C in sterile sample bags and transported frozen to Oregon State University.

Scanning Electron Microscopy

Excess pieces crushed for culture experiments and not used were preserved for examination by scanning electron microscopy. Rock chips were preserved in 1% glutaraldehyde solution and maintained at 4°C.

Total Organic Carbon

One-third of each sample of hard rock collected for microbiology was placed in a glass jar that had been baked at 550°C for 12 hr. The glass jars were sealed and stored at 4°C for postcruise total organic carbon analysis.

Sediments

Sampling

Sediment samples were collected using sterile 50-mL tubes. Sample weight was calculated by subtracting collection tube weight.

Direct Counts and Enrichment Cultures

Ten milliliters of autoclaved and filter sterilized artificial seawater (ASW) was added to separate tubes for direct counts and enrichment cultures. Tubes were vortexed by hand until the mud pellets were in solution. Tubes were then allowed to sit at room temperature until settling occurred and clear ASW was visible. Aliquots of the ASW were then used for direct count analysis and culturing by spread plate technique using R2A. Direct counts were reported as counts per milliliter of cleared ASW following mixing and settling. Cultures results were reported as colony forming units per gram of mud after adjusting for the added ASW.

Seawater and Water Samples

Surface Seawater

Surface seawater samples were collected using a sterile flask lowered from the bow of the ship, to avoid the ship's wastewater and cooling water. One liter of seawater was filtered through a 0.2- μm vacuum filtration rig from each drill site. The filter was preserved with a 20% sterile glycerol and 1 \times phosphate buffered saline (PBS) solution, then was frozen at -80°C . The filters were used for shore-based DNA analysis.

Bottom Water

Bottom water samples were taken at the drill site with the water sampling temperature probe (WSTP). Prior to deployment, the WSTP was flushed with 10% bleach to sterilize the equipment and then flushed with filtered (0.2- μm pore size) distilled water. The coil and overflow tank of the WSTP contained filtered distilled water at the time of deployment. Water from the coil reservoir was extracted with forced air flow. The water samples from both the coil and overflow reservoirs were filtered and the filters were preserved with a 20% sterile glycerol and 1 \times PBS solution and frozen for DNA extraction on shore at Oregon State University.

Contamination Tests

Two types of tracer tests were conducted to determine the level of contamination of samples recovered by drilling: perfluorocarbon tracer (PFT) and fluorescent microspheres. Detailed methods for these tests are described in "Materials and Methods" in "Methods for Quantifying Potential Microbial Contamination During Deep Ocean Coring" (Smith et al., 2000).

Perfluorocarbon Tracer

Perfluoro(methylcyclohexane) was used as a liquid tracer within the borehole circulation fluid (seawater). The PFT was not diluted prior to introduction into the circulation fluid. The PFT was injected into the drilling fluid automatically and achieved a final concentration of 1 mg/L. The tracer was pumped early enough to reach the bit before the coring began and maintained a steady concentration throughout the drill string.

Once the cores arrived on deck, several small pieces were placed into headspace vials and sealed to confirm that the PFT reached the core.

Next, the PFT was flamed off the surface of the core with a propane torch to prevent spreading the PFT to the interior while breaking up the core. The exterior rock was chipped away, and pieces of the interior were crushed and sealed in headspace vials. The headspace vials and gas-tight syringes were heated to 70°C. Five milliliters of headspace gas was injected into a Hewlett-Packard 5890 GC. Volume of drilling fluid in the core was calculated based on PFT concentration in the rocks and the concentration in the drilling fluid.

Microspheres

Yellow-green fluorescent carboxylate microspheres, 0.518 μm (± 0.021 μm) in diameter, were used as a particulate tracer. The microspheres emit bright green fluorescence when observed under epifluorescence microscopy using a blue filter set. To achieve an approximate concentration of 10^{10} microspheres/mL, 2 mL of the microsphere suspension (2.86% solids in deionized water) was diluted to 40 mL with nanopure water. The diluted solution was placed in an ultrasonic bath to disrupt aggregates. The diluted solution was then poured into a plastic bag, excess air was expelled, and the bag was heat sealed and wedged into a recess in the top of an auxiliary core catcher insert supported by the core catcher fingers. Core entering the barrel ruptured the bag, dispersing the microspheres into the core barrel.

Pieces of rock close to the top of the core were selected to maximize the probability of finding the microspheres. The surface of the rock was washed with distilled water, and aliquots of the wash water were filtered onto polycarbonate filters. Rock thin sections were then prepared with no special precautions. A Zeiss Axiophot epifluorescence microscope with a 100-W mercury lamp, a blue filter set, and a 100 \times Plan-Neofluar oil-immersion objective was used to check for presence of microspheres.

Atmospheric Microbiology

The primary objectives of atmospheric microbiology studies during Leg 209 were to determine what types of microorganisms and pollutants were being transported across the Atlantic in African dust clouds and how nutrients in these clouds impact primary productivity in the tropical mid-Atlantic. To do this, both membrane filtration and liquid impingement were used to collect volumes of air on a daily basis. The air samples were then used to isolate and identify culturable and non-culturable bacteria, fungi, and viruses from the atmosphere. Contamination from shipboard air was minimized by collecting atmospheric samples on the windward side of the ship.

Atmospheric condition values were obtained using National Aeronautics and Space Administration (NASA) SeaWiFS global images and a photo manipulation software package (Ulead Photo Impact) for the purpose of graphing atmospheric conditions in relation to microbiology data. SeaWiFS images were opened in the software package and a 3° latitude \times 3° longitude box was superimposed on the sample site ($\sim 15^\circ\text{N}$, 45°W). Image pixel tone for that area was then calculated using an image tone mapper. The value was calculated based on the pixel tone sum graphed by the software's tone mapper (bell-shaped curves within a 5 pixel \times 5 pixel box). Baseline values were obtained by taking 10-tone map measurements of clear, light cloud cover, heavy cloud

cover, light dust, and heavy dust conditions using a series of SeaWiFS images (20 May–23 May 2003). Baseline measurement ranges were

- Clear = 0.4–5.4,
- Light cloud = 1.8–8.17,
- Light dust = 8.61–13.05,
- Heavy dust = 11.25–14.4, and
- Heavy cloud = 14.4–21.6.

See Figure F11 for a graph of baseline values.

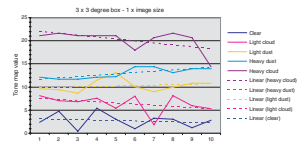
Membrane Filtration

A portable membrane filtration unit was used to take samples on the windward side of the ship (Fig. F12). Presterilized filter housings containing 47-mm-diameter, 0.2- μm pore size filter membranes were used to collect all air samples (Fisher Scientific, Atlanta, Georgia, 09-74030G) in duplicate. The filter housings were removed from their respective sterile bags and placed on an analytical filter manifold. The lids were removed, and vacuum was applied using a vacuum pump for a set period of time. Air flow rates through the filters were 6.5 L/min for 40 min per sample. To control for handling contamination, an additional filter housing was removed from its bag, placed on the manifold, and allowed to sit for 1 min without removing the lid or turning on the vacuum. Filter housings were then removed from the manifold; the lids were sealed with parafilm and replaced in their respective bags for transport to the ship laboratory. R2A agar (Fisher Scientific, Atlanta, Georgia, DF1826-17-1) was used for microbial culture-based analysis. The sample filters were placed on R2A agar plates, sample side up, incubated in the dark at room temperature ($\sim 21^\circ\text{C}$), and monitored for growth over a 48-hr period. Fungal and bacterial colonies were separated by isolation streaking onto fresh plates of R2A. Once isolated, colonies were grown overnight at room temperature in tryptic soy broth (Fisher Scientific, Atlanta, Georgia, DF0370-17-3). The following day, 1 L of each culture was transferred to a sterile cryogenic storage tube containing 200 μL of sterile glycerol and stored at -80°C for shore-based identification using DNA sequencing of each isolate 16S (bacterial) or 18S (fungal) ribosomal DNA (rDNA) sequences.

Liquid Impinger

A sterile liquid impinger vial containing 30 mL of autoclaved 0.5-M tris buffer (pH = 7.5) and a LaMotte (Chestertown, Maryland) air sampling pump was used to collect samples (Fig. F13). The assembled impinger unit was set to pump 1.5 L/min and allowed to run for 8 hr. After the sample collection was complete, the unit was transported to the laboratory for processing. Five milliliters of sample (in duplicate) was used for onboard microbial direct count assay using 0.02- μm pore size glass fiber filters, SYBR gold nucleic acid stain (Molecular Probes, Inc.), and epifluorescent microscopy. Another 5 mL of sample was preserved with 0.02- μm filtered formaldehyde and stored in a refrigerator at 4°C for shore-based analysis of the viral community using transmission electron microscopy. The remaining volume of sample was transferred to a sterile 15-mL tube and frozen at -80°C for shore-based analysis of bacterial community DNA using the polymerase chain reaction coupled with denaturing gradient gel electrophoresis and pathogen screening.

F11. Baseline values for classifying SeaWiFS images, p. 53.



F12. Portable membrane filtration apparatus, p. 54.



F13. Portable liquid impinger, p. 55.



Water Samples

Surface water samples were collected each day at 1400 hr by lowering a sterile 50-mL tube from the bow of the *JOIDES Resolution* to prevent shipborne contamination. Ten milliliters of the sample (in duplicate) was filtered through a 0.02- μm glass filter using a sterile glass filter funnel. After filtration, the microorganisms on the filter surface were stained with SYBR gold nucleic acid stain. A negative control was used to account for microbial contamination of staining reagents, handling, and glassware. Ten microscope fields per sample were counted, and the averages of the field counts in the duplicate samples were used to determine total numbers of bacteria and viruses per milliliter of sample, via epifluorescent microscopy. Direct counts were also performed on aliquots of bottom water samples.

Airborne Metals and Pollution

Samples for the analysis of metals and chemical pollutants were collected using a roofed four-place air sample unit (Fig. F14). The unit was placed at the crown of the ship drill tower, and samples were collected over three 1-week periods. The unit was turned off to prevent aerosol contamination during certain phases of drilling operations. Air sampling was based on conventional methods comparable to the U.S. Environmental Protection Agency's method TO-4A and related methods for semivolatile organic compounds, or IO-3, methods for determining inorganic species in suspended particulate matter. Four sampler cartridges were deployed for contaminant analyses: one for current-use pesticides, polyaromatic hydrocarbons, and other organic chemicals; one for antibiotics and pharmaceuticals; one for dioxins; and one for trace metals. Sampling trains for organic compounds consisted of a glass-fiber filter followed by two polyurethane foam plugs in series contained in a Teflon cartridge. Total air concentrations were determined by combined analysis of vapor and particle phases to achieve low detection levels. Quartz fiber filters were used to collect atmospheric particles for trace metal analysis. Field equipment blank samples were collected at each site for each sample type. Air pump flow rates through each filter type were recorded at the beginning and end of each sampling period.

F14. Air sampler, p. 56.



DOWNHOLE MEASUREMENTS

The downhole logging program during Leg 209 was specifically designed for determining the orientation of faults and fractures as well as characterizing deformation and alteration features of the upper mantle and lower crustal rock sequences drilled north and south of the 15° 20'N fracture zone. Several wireline and logging-while-drilling (LWD) tools were deployed, as described below.

Wireline Logging Tools and Tool Strings

Individual logging tools were joined together into tool strings so that several measurements can be made during each logging run. The tool strings were lowered to the bottom of the borehole on a wireline cable, and data were logged as the tool string was pulled back up the hole. Repeat runs were made to improve coverage and confirm the accuracy of log data. Not all tool strings were run in each hole; refer to individual

site chapters for details of logging strings deployed at each site. During Leg 209, the following logging strings were successfully deployed in Holes 1272A and 1275D (Fig. F15; Table T11):

1. The triple combination (triple combo) string (resistivity, density, and porosity measurements), which consists of the Hostile Environment Gamma Ray Sonde (HNGS), the Phasor Dual Induction and Spherically Focused Resistivity Tool (DIT-E/SFR), the Hostile Environment Litho-Density Sonde (HLDS), and the Accelerator Porosity Sonde (APS). The Lamont-Doherty Earth Observatory (LDEO) high-resolution Temperature/Acceleration/ Pressure tool (TAP) was attached at the bottom of this tool string.
2. The Formation MicroScanner (FMS)-sonic tool string, which consists of the FMS, the General Purpose Inclinerometer Tool (GPIT), the Scintillation Gamma Ray Tool (SGT), and the Dipole Sonic Imager (DSI) tool.

Principles and Uses of the Wireline Logging Tools

The properties measured by each tool, sampling intervals, and vertical resolutions are summarized in Table T11. Explanations of tool name acronyms and their measurement units are summarized in Table T12. More detailed descriptions of individual logging tools and their geological applications can be found in Ellis (1987), Goldberg (1997), Rider (1996), Schlumberger (1989, 1994), Serra (1984, 1986, 1989), and the LDEO–Borehole Research Group (BRG) Wireline Logging Services Guide (WLSG) (2001).

Gamma Ray Tools

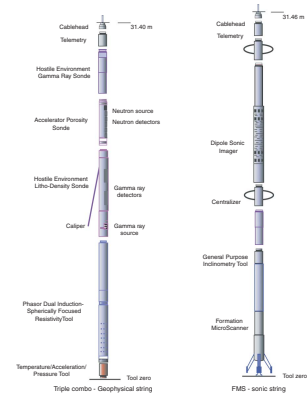
The HNGS measures natural gamma radiation from isotopes of potassium, thorium, and uranium and uses a five-window spectroscopic analysis to determine concentrations of radioactive potassium (in weight percent), thorium (in parts per million), and uranium (in parts per million). The HNGS uses two bismuth germanate scintillation detectors for gamma ray detection with full spectral processing. The HNGS also provides a measure of the total gamma ray emission (SGR) and uranium-free or computed gamma ray emission (CGR) that are measured in American Petroleum Institute units (gAPI). The HNGS response is influenced by the borehole diameter.

Processing of HNGS data at LDEO-BRG corrects for borehole diameter variations. The SGT uses a sodium iodide scintillation detector to measure the total natural gamma ray emission, combining the spectral contributions of potassium, uranium, and thorium concentrations in the formation. The SGT is not a spectral tool but provides high-resolution total gamma ray data for depth correlation between logging strings. It is included in all tool strings (except the triple combo, where the HNGS is used) to provide a reference log to correlate depth between different logging runs.

Hostile Environment Litho-Density Tool

The HLDS consists of a radioactive cesium (^{137}Cs) gamma ray source (622 keV) and far- and near-gamma ray detectors mounted on a shielded skid, which is pressed against the borehole wall by a hydraulically activated eccentricizing arm. Gamma rays emitted by the source

F15. Configuration of the wireline tool, p. 57.



T11. Wireline and LWD tool specifications, p. 73.

T12. Acronyms and units for wireline tools, p. 74.

experience both Compton scattering and photoelectric absorption. The number of scattered gamma rays that reach the detectors is directly related to the number of electrons in the formation, which is related to bulk density. Porosity may also be derived from this bulk density if the matrix density is known.

The HLDS also measures the photoelectric effect factor (PEF) caused by absorption of low-energy gamma rays. Photoelectric absorption occurs when gamma rays reach <150 keV after being repeatedly scattered by electrons in the formation. As the PEF depends on the atomic number of the elements in the formation, it is essentially independent of porosity. Thus, the PEF varies according to the chemical composition of the formation. Some examples of PEF values are provided in Table T13. The PEF values can be used in combination with HNGS curves to identify different types of clay minerals. Coupling between the tool and borehole wall is essential for high-quality HLDS logs. Poor contact results in underestimation of density values. Both density correction and caliper measurement of the hole are used to check the contact quality.

T13. PEF of igneous and alteration minerals, p. 75.

Accelerator Porosity Sonde

The APS consists of a minitron neutron generator that produces fast neutrons (14.4 MeV) and five neutron detectors (four epithermal and one thermal) positioned at different spacings along the tool. The tool is pressed against the borehole wall by an eccentricizing bow-spring. Emitted high-energy (fast) neutrons are slowed down by collisions with atoms. The amount of energy lost per collision depends on the relative mass of the nucleus with which the neutron collides. The largest energy loss occurs when the neutron strikes a nucleus of equal mass, such as hydrogen, which is mainly present in pore water. Once neutrons degrade to thermal energies (0.025 eV), they may be captured by the nuclei of silicon, chlorine, boron, and other elements, with the associated emission of a gamma ray. The neutron detectors record both the numbers of neutrons arriving at various distances from the source and the neutron arrival times, which act as a measure of formation porosity. However, hydrogen bound in minerals such as clays or in hydrocarbons also contributes to the measurement, so the raw porosity value is often an overestimate.

Dual Induction Tool and Spherically Focused Resistivity

The DIT-E provides three different measurements of electrical resistivity, each with a different depth of penetration into the formation. Two induction devices (deep and medium resistivity) transmit high-frequency alternating currents through transmitter coils, creating magnetic fields that induce secondary (Foucault) currents in the formation. These ground-loop currents produce new inductive signals, proportional to the conductivity of the formation, which are measured by the receiving coils. The measured conductivities are then converted to resistivity. A third device, a spherically focused resistivity instrument, gives higher vertical resolution, as it measures the current necessary to maintain a constant voltage drop across a fixed interval.

High-Resolution Temperature/Acceleration/Pressure Tool

The TAP is a “dual-application” logging tool (i.e., it can operate either as a wireline tool or as a memory tool using the same sensors).

Data acquisition electronics are dependent on the purpose and required precision of logging data. During Leg 209, the TAP was deployed as a memory tool in low-resolution mode; data were stored in the tool and downloaded after the logging run was completed. Temperatures determined using the TAP do not necessarily represent in situ formation temperatures because water circulation during drilling will have disturbed temperature conditions in the borehole.

Dipole Sonic Imager Tool

The monopole source of the DSI generates compressional, shear, and Stoneley waves into hard formations. The configuration of the DSI also allows recording of cross-dipole waveforms. In many cases the dipole sources can also provide estimates of shear wave velocity in hard rocks better than or equivalent to the monopole source. These combined modes can be used to estimate shear-wave splitting caused by preferred mineral and/or structural orientation in consolidated formations. A low-frequency (80 Hz) source enables Stoneley waveforms to be acquired as well.

The DSI measures the transit times between sonic transmitters and an array of eight receiver groups with 15-cm spacing, each consisting of four orthogonal elements that are aligned with the dipole transmitters. During acquisition, the output from these 32 individual elements are differenced or summed appropriately to produce in-line and cross-line dipole signals or monopole-equivalent (compressional and Stoneley) waveforms, depending on the operation modes. The detailed description of tool configuration and data processing are described in the Leg 174B *Initial Reports* volume (Shipboard Scientific Party, 1998). The velocity data from the DSI together with the formation density can be used to generate a synthetic seismogram.

Formation MicroScanner

The FMS produces high-resolution images of borehole wall micro-resistivity that can be used for detailed lithostratigraphic or structural interpretation. This tool has four orthogonally oriented pads, each with 16 button electrodes that are pressed against the borehole walls. Good contact with the borehole wall is necessary for acquiring good-quality data. Approximately 30% of a borehole with a diameter of 25 cm is imaged during a single pass. Coverage may be increased by a second run. The vertical resolution of FMS images is ~5 mm. The resistivity measurements are converted to color or gray-scale images for display. In site chapters in this volume, local contrasts in FMS images were improved by applying dynamic normalization to the FMS data. A linear gain is applied, which keeps a constant mean and standard deviation within a sliding window of 1 m. FMS images are oriented to magnetic north using the GPIT, assuming that the GPIT can locate magnetic north in magnetite-rich environments (see "General Purpose Inclinometer Tool" below for more details). This method allows the dip and strike of interpreted geological features intersecting the hole to be measured from processed FMS images.

General Purpose Inclinometer Tool

The GPIT is included in the FMS-sonic tool string to calculate tool acceleration and orientation during logging. Tool orientation is defined

by three parameters: tool deviation, tool azimuth, and relative bearing. The GPIT utilizes a three-axis inclinometer and a three-axis fluxgate magnetometer to record the orientation of the FMS images as the magnetometer records the magnetic field components (F_x , F_y , and F_z). Corrections for cable stretching and/or ship heave using acceleration data (A_x , A_y , and A_z) allow precise determinations of log depths. A hydraulic wireline heave compensator designed to adjust for rig motion during logging operations minimizes ship heave.

In magnetic-rich rocks such as serpentinites or oxide-rich gabbros, there is some uncertainty to the orientation of the GPIT. We compared downhole GPIT data with shipboard determinations of remanent magnetization and magnetic susceptibility. In this way, we were able to evaluate whether assumptions about remanence (no tectonic rotation around a vertical axis since magnetization), relative abundance of magnetic minerals, and GPIT measurements (magnetometer can determine the direction of magnetic north) yielded consistent results (see the “[Site 1272](#)” and “[Site 1275](#)” chapters).

Logging Data Flow and Processing

Data for each wireline logging run were recorded and stored digitally and monitored in real time using the Schlumberger MAXIS 500 system. After logging was completed in each hole, data were transferred to the shipboard downhole measurements laboratory (DHML) for preliminary processing and interpretation. FMS image data were interpreted using Schlumberger's Geoframe software package (version 3.8).

Logging data were also transmitted to LDEO-BRG using a satellite high-speed data link for processing soon after each hole was logged. Data processing at LDEO-BRG consists of

1. Depth-shifting all logs relative to a common datum (i.e., in mbsf),
2. Corrections specific to individual tools, and
3. Quality control and rejection of unrealistic or spurious values.

Once processed at LDEO-BRG, logging data were transmitted back to the ship, providing near-real time data processing. Processed data were then replotted on board (see the “Downhole Measurements” sections in each site chapter). Further postcruise processing of the logging data from the FMS is performed at LDEO-BRG. Postcruise-processed data (in ASCII) are available directly from the LDEO-BRG Internet World Wide Web site at www.ldeo.columbia.edu/BRG/ODP/DATABASE/. A summary of “logging highlights” is posted on the LDEO-BRG Web site at the end of each leg.

Wireline Log Data Quality

Logging data quality may be seriously degraded by changes in hole diameter and in sections where the borehole diameter greatly decreases or is washed out. Deep-investigation measurements such as resistivity and sonic velocity are least sensitive to borehole conditions. Nuclear measurements (density and neutron porosity) are more sensitive because of their shallower depth of investigation and the effect of drilling fluid volume on neutron and gamma ray attenuation. Corrections can be applied to the original data in order to reduce these effects. HNGS and SGT data provide a depth correlation between logging runs. Logs

from different tool strings may, however, still have depth mismatches caused by either cable stretch or ship heave during recording.

Logging While Drilling

During Leg 209, two LWD resistivity tools were available: the Resistivity-at-the-Bit (RAB) and Resistivity-at-the-Bit while Coring (RAB-C) systems. Only the RAB-C was used for Hole 1275C. Schlumberger Drilling and Measurements provided these tools under contract with LDEO-BRG. LWD surveys have been successfully conducted during eight previous ODP legs: Leg 156 (Shipley, Ogawa, Blum, et al., 1995), Leg 170 (Kimura, Silver, Blum, et al., 1997), Leg 171A (Moore, Klaus, et al., 1998), Leg 174A (Austin, Christie-Blick, Malone, et al., 1998), Leg 188 (O'Brien, Cooper, Richter, et al., 2001), Leg 193 (Binns, Barriga, Miller, et al., 2002), Leg 196 (Mikada, Becker, Moore, Klaus, et al., 2002), and Leg 204 (Tréhu, Bohrmann, Rack, Torres, et al., 2003).

LWD tools measure in situ formation properties with instruments that are located in the drill collars immediately above the drill bit. LWD data were recorded into downhole computer memory and retrieved when the tools reach the surface. Measurements were made shortly after the hole is drilled and before the adverse effects of continued drilling or coring operations. Fluid invasion into the borehole wall was also reduced relative to wireline logging because of the shorter elapsed time between drilling and taking measurements.

The LWD equipment is battery powered and uses nonvolatile memory chips to store logging data until they are downloaded. The LWD tools took measurements at evenly spaced time intervals and were synchronized with a system on the drilling rig that monitors time and drilling depth. After drilling, the LWD tools were retrieved and the data were downloaded from each tool using a DB-25 485 cable serial link to a processing computer in the DHML. Synchronization of the uphole and downhole clocks allows merging of the time-depth data (from the surface system) and the downhole time-measurement data (from the tools) into depth-measurement data files. The resulting depth-measurement data were transferred to the processing systems in the DHML for reduction and interpretation.

Depth Tracking Systems

Unlike wireline tools, which record data vs. depth, LWD tools record data vs. time. Schlumberger's Drilling and Measurements Integrated Drilling Evaluation and Logging system (IDEAL) records the time and the depth of the drill string below the rig floor. LWD operations aboard the *JOIDES Resolution* require accurate and precise depth tracking and the ability to independently measure and evaluate the movement of the following:

1. Position of the traveling block in the derrick,
2. Heave of the vessel by the action of waves/swells and tides, and
3. Action of the motion compensator.

Resistivity-at-the-Bit Tools

RAB tools provide resistivity measurements of the formation and electrical images of the borehole wall, similar to the Formation Micro-Scanner but with complete coverage of the borehole walls and lower

vertical and horizontal resolution. In addition, the RAB tool contains a thallium-doped sodium iodine scintillation detector that provides a total gamma ray measurement (Fig. F16). Because a caliper log is not available without other LWD measurements, the influence of the shape of the borehole on the log responses can only be estimated by a qualitative comparison of the shallow, medium, and deep button images.

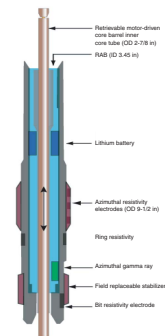
The RAB tools are connected directly above the drill bit, and they use the lower portion of the tool and the bit as a measuring electrode. This allows the tool to provide a bit resistivity measurement with a vertical resolution just a few inches longer than the length of the bit. A 2.5-cm electrode is located 91 cm from the bottom of the tool and provides a focused lateral resistivity measurement (RRING) with a vertical resolution of 5 cm. The characteristics of RRING are independent of where the RAB tool is placed in the bottom-hole assembly (BHA), and its depth of investigation is ~18 cm. In addition, button electrodes provide shallow-, medium-, and deep-focused resistivity measurements as well as azimuthally oriented images. These images can then reveal information about formation structure and lithologic contacts. The button electrodes are ~2.5 cm in diameter and reside on a clamp-on sleeve. The buttons are longitudinally spaced along the RAB tool to render staggered depths of investigation of ~2.5, 7.6, and 12.7 cm. The tool's orientation system uses the Earth's magnetic field as a reference to determine the tool position with respect to the borehole as the drill string rotates, thus allowing both azimuthal resistivity and gamma ray measurements *provided that azimuth can be measured correctly in serpentinized peridotites with a few weight percent magnetite*. Resistivity measurements are acquired with ~6° resolution as the RAB tool rotates, and gamma ray profiles are acquired in quadrants and can only be referenced to the top of the hole. The sampling interval for each resistivity measurement is shown in Table T11.

Two RAB tool collar configurations were designed for use during Leg 209. The RAB tool used in the 6¾-in LWD BHA is called the GeoVision resistivity, which is the most recent upgrade of the tool, and was not used during Leg 209. A RAB-8 tool collar configuration for use with a larger 8-in-diameter BHA was deployed at Site 1275. The design is intended for use in conjunction with a modified motor-driven core barrel core-liner system, allowing RAB measurements to be made while coring (RAB-C; Fig. F16). Hole 1275C was the second attempt to core and record LWD data simultaneously (the first was during Leg 204). The RAB-8 tool was deployed alone in the BHA, and the standard 25-cm-diameter rotary bit was used. The diameter of the measuring button sleeve for the RAB-8 tool is 24.1 cm; thus, borehole size resistivity correction factors are negligible for all of the RAB-8 measurements, including the shallow button resistivity. The RAB-8 tool provides electrical images of the borehole wall, similar to the FMS, and allows for recovering cores with a 6.51 cm diameter. The vertical resolution of the images is lower than that of the FMS (Table T11) but the images have complete coverage of the borehole walls.

RAB Programming

All logging data were collected at a minimum vertical sampling density of 15 cm whenever possible; hence, a balance must be determined between the rate of penetration (ROP) and the sampling rate. This relationship depends on the recording rate, the number of data channels to record, and the memory capacity of the LWD tool. The RAB-8 tool was

F16. Configuration of the RAB-8 tool, p. 58.



programmed with a sampling rate of 10 s for data acquisition and a memory capacity of 5 MB. The maximum ROP allowed to produce one sample per 15.24 cm interval is given by the equation

$$\text{ROP (m/hr)} = 548/\text{sample rate.}$$

This relationship gives 55 m/hr maximum ROP for the RAB-8 tool. During Leg 209, the target ROP was 1–5 m/hr, roughly 1%–5% of the maximum allowable for the RAB-8 tool. These reduced rates improve the maximum vertical resolution of the resistivity images to 3 cm. Under this configuration, the RAB-8 tool was able to record as long as 30 hr, which was sufficient to complete the LWD operations at Site 1275 (see “[Downhole Measurements](#),” p. 37, in the “Site 1275” chapter).

Bit Resistivity Measurements

For the bit resistivity measurements, a lower transmitter produces a current and a monitoring electrode located directly below the ring electrode measures the current returning to the collar. The resultant resistivity measurement is termed RBIT, and its depth of investigation is ~30.5 cm.

Ring Resistivity Measurements

The upper and lower transmitters produce currents in the collar that meet at the ring electrode. The sum of these currents is then focused radially into the formation. These current patterns can become distorted depending on the strength of the fields produced by the transmitters and the formation around the collar. Therefore, the RAB-8 tool uses a cylindrical focusing technique that takes measurements in the central and lower monitor coils to reduce distortion and create an improved ring response. The ring electrode is held at the same potential as the collar to prevent interference with the current pattern. The current required for maintaining the ring at the required potential is then measured and related to the resistivity of the formation. Because the ring electrode is narrow (~4 cm), the result is a measurement (RRING) with 5-cm vertical resolution.

Button Resistivity Measurements

The button electrodes function the same way as the ring electrode. Each button is electrically isolated from the body of the collar but is maintained at the same potential to avoid interference with the current field. The amount of current required to maintain the button at the same potential is related to the resistivity of the mud and formation. The buttons are 4 cm in diameter, and the measurements (RBUTTON) can be acquired azimuthally as the tool rotates within 56 sectors to produce a borehole image.

Interpreting Structure from RAB and FMS Images

Structural data were determined from RAB images using Schlumberger’s GeoFrame software. GeoFrame presents RAB data as a planar “unwrapped” 360° resistivity image of the borehole with depth. The image orientation is referenced to north, which is measured by the magnetometers inside the tool, and the hole is assumed to be vertical. Hori-

zontal features appear horizontal on the images, whereas planar, dipping features are sinusoidal in aspect. Sinusoids are interactively fitted to beds and fractures to determine their dip and azimuth, and the data are exported from GeoFrame for further analysis.

Methods of interpreting structure and bedding differ considerably between core analysis, wireline FMS images, and RAB image analysis. Resolution is considerably lower for RAB image interpretation (3 cm at best, compared with <1 mm within cores and 0.5 cm for FMS images), and therefore identified features are likely to be different in scale. For example, microfaults (width < 1 mm) and shear bands (width = 1–2 mm or up to 1 cm) can only be interpreted from core analysis and, sometimes, from FMS data. This should be considered when directly comparing reports. The RAB tool provides 360° coverage at a lower resolution; FMS provides higher-resolution data, but coverage is restricted to ~30% of the borehole wall. Fractures can be identified in RAB images by their anomalous resistivity or conductivity and from contrasting dip relative to surrounding foliation trends. Differentiating between fractures and foliation planes can be problematic, particularly if both are steeply dipping and have similar orientations.

During processing, quality control of the data is mainly performed by cross-correlation of all logging data. Large (>12 in) and/or irregular borehole diameter affects most recordings, particularly the HLDS, which requires eccentricity and good contact with the borehole wall. Hole deviation can also negatively affect the data; the FMS, for example, is not designed to be run in holes with >10° deviation, as the tool weight might cause the caliper to close.

FMS image processing is required to convert the electrical current in the formation, emitted by the FMS button electrodes, into a gray or color-scale image representative of the conductivity changes. This is achieved through two main processing phases: data restoration and image display. During the data restoration process, speed corrections, image equalization, button correction, emitter exciter (EMEX) voltage correction, and depth-shifting techniques are applied to the data.

Speed corrections use the data from the z-axis accelerometer to correct the vertical position of the data for variations in the speed of the tool (i.e., GPIT speed correction), including tool sticking and slipping. In addition, an image-based speed correction is also applied to the data. This correction checks the GPIT speed correction. If the correction is successful, the readings from the two rows of buttons on the pads will line up. If not, the readings will be offset from each other, creating a zigzag effect on the image.

Image equalization is the process whereby the average response of all the buttons of the tool are rendered approximately the same over large intervals, to correct for various tool and borehole effects that affect individual buttons differently. These effects include differences in the gain and offset of the pre-amplification circuits associated with each button and differences in contact with the borehole wall between buttons on a pad and between pads. If the measurements from a particular button are unreasonably different from adjacent buttons (e.g., “dead buttons”) over a particular interval, they are declared faulty, and the defective trace is replaced by traces from adjacent good buttons. The button current response is controlled by the EMEX voltage, which is applied between the button electrode and the return electrode. The EMEX voltage is regulated to keep the current response within the operating range. The button response is divided by the EMEX voltage, and, as a

result, the response corresponds more closely to the conductivity of the formation.

Each of the logging runs are depth-matched to a common scale by means of lining up distinctive features of the natural gamma log from each of the tool strings. If the reference-logging run is not the FMS tool string, the specified depth shifts are applied to the FMS images. The position of data located between picks is computed by linear interpolation.

Once the data are processed, both static and dynamic images are generated. In static normalization, a histogram equalization technique is used to obtain the maximum quality image. In this technique, the resistivity range of the entire interval of good data is computed and partitioned into 256 color levels. This type of normalization is best suited for large-scale resistivity variations. The image can be enhanced when it is desirable to highlight features in sections of the borehole where resistivity contrasts are relatively low when compared with the overall resistivity range in the section. This enhancement is called dynamic normalization, and by rescaling the color intensity over a smaller interval, the contrast between adjacent resistivity levels is enhanced. It is important to note that with dynamic normalization, resistivities in two distant sections of the hole cannot be directly compared with each other. A 2-m normalization interval was used.

The FMS images are displayed as an unwrapped borehole cylinder with a circumference derived from the bit size. Several passes can be oriented and merged together on the same presentation to give additional borehole coverage where the tool pads followed a different track during the second logging pass. A dipping plane in the borehole can be displayed as a sinusoid on the image and the amplitude of this sinusoid is proportional to the dip of the plane. The images are oriented with respect to north; hence, the strike of dipping features can also be determined.

REFERENCES

- ASTM, 1989. *Annual Book of ASTM Standards for Soil and Rock: Building Stones* (Vol. 4.08): *Geotextiles*: Philadelphia (Am. Soc. Testing and Mater.).
- Austin, J.A., Jr., Christie-Blick, N., Malone, M.J., et al., 1998. *Proc. ODP, Init. Repts.*, 174A: College Station, TX (Ocean Drilling Program).
- Bach, W., Erzinger, J., Alt, J.C., and Teagle, D.A.H., 1996. Chemistry of the lower sheeted dike complex, Hole 504B (Leg 148): influence of magmatic differentiation and hydrothermal alteration. In Alt, J.C., Kinoshita, H., Stokking, L.B., and Michael, P.J. (Eds.), *Proc. ODP, Sci. Results*, 148: College Station, TX (Ocean Drilling Program), 39–55.
- Binns, R.A., Barriga, F.J.A.S., Miller, D.J., et al., in press. *Proc. ODP, Init. Repts.*, 193 [CD-ROM]. Available from: Ocean Drilling Program, Texas A&M University, College Station TX 77845-9547, USA.
- Blum, P., 1997. Physical properties handbook: a guide to the shipboard measurement of physical properties of deep-sea cores. *ODP Tech. Note*, 26 [Online]. Available from World Wide Web: <<http://www-odp.tamu.edu/publications/tnotes/tn26/INDEX.HTM>>. [Cited 2003-07-06]
- Bouchez, J.L., Delas, C., Gleizes, G., Nedelec, A., and Cuney, M., 1992. Submagmatic microfractures in granites. *Geology*, 20:35–38.
- Boyce, R.E., 1976. Definitions and laboratory techniques of compressional sound velocity parameters and wet-water content, wet-bulk density, and porosity parameters by gravimetric and gamma-ray attenuation techniques. In Schlanger, S.O., Jackson, E.D., et al., *Init. Repts. DSDP*, 33: Washington (U.S. Govt. Printing Office), 931–958.
- Cannat, M., Karson, J.A., Miller, D.J., et al., 1995. *Proc. ODP, Init. Repts.*, 153: College Station, TX (Ocean Drilling Program).
- Cannat, M., Mével, C., and Stakes, D., 1991. Normal ductile shear zones at an oceanic spreading ridge: tectonic evolution of Site 735 gabbros (southwest Indian Ocean). In Von Herzen, R.P., Robinson, P.T., et al., *Proc. ODP, Sci. Results*, 118: College Station, TX (Ocean Drilling Program), 415–429.
- Dick, H.J.B., Meyer, P.S., Bloomer, S., Kirby, S., Stakes, D., and Mawer, C., 1991. Lithostratigraphic evolution of an in-situ section of oceanic Layer 3. In Von Herzen, R.P., Robinson, P.T., et al., *Proc. ODP, Sci. Results*, 118: College Station, TX (Ocean Drilling Program), 439–538.
- Dick, H.J.B., Natland, J.H., Miller, D.J., et al., 1999. *Proc. ODP, Init. Repts.*, 176: College Station, TX (Ocean Drilling Program).
- Ellis, D.V., 1987. *Well Logging for Earth Scientists*: New York (Elsevier).
- Gillis, K., Mével, C., Allan, J., et al., 1993. *Proc. ODP, Init. Repts.*, 147: College Station, TX (Ocean Drilling Program).
- Goldberg, D., 1997. The role of downhole measurements in marine geology and geophysics. *Rev. Geophys.*, 35:315–342.
- Govindaraju, K., 1994. 1994 compilation of working values and sample description for 383 geostandards. *Geostand. Newsl.*, 18.
- Hext, G., 1963. The estimation of second-order tensors, with related tests and designs. *Biometrika*, 50:353–357.
- Hirth, G., and Kohlstedt, D.L., 1995. Experimental constraints on the dynamics of the partially molten upper mantle: deformation in the diffusion creep regime. *J. Geophys. Res.*, 100:1981–2001.
- Kimura, G., Silver, E.A., Blum, P., et al., 1997. *Proc. ODP, Init. Repts.*, 170: College Station, TX (Ocean Drilling Program).
- Kirschvink, J.L., 1980. The least-squares line and plane and the analysis of palaeomagnetic data. *Geophys. J. R. Astron. Soc.*, 62:699–718.
- Kobayashi, Y., 1974. Anisotropy of thermal diffusivity in olivine, pyroxene and dunite. *J. Phys. Earth*, 22:35–373.

- Kretz, O., 1983. Symbols for rock-forming minerals. *Am. Mineral.*, 68:277–279.
- Lamont-Doherty Earth Observatory–Borehole Research Group, 2001. *ODP Logging Services Electronic Manual*, Version 2.0 [Online]. Available from World Wide Web: <<http://www.ldeo.columbia.edu/BRG/ODP/LOGGING/MANUAL/index.html>>. [Cited 2003-02-15]
- Means, W.D., and Park, Y., 1994. New experimental approach to understanding igneous texture. *Geology*, 22:323–326.
- Mikada, H., Becker, K., Moore, J.C., Klaus, A., et al., 2002. *Proc. ODP, Init. Repts.*, 196 [CD-ROM]. Available from: Ocean Drilling Program, Texas A&M University, College Station TX 77845-9547, USA.
- Moore, J.C., Klaus, A., et al., 1998. *Proc. ODP, Init. Repts.*, 171A [CD-ROM]. Available from: Ocean Drilling Program, Texas A&M University, College Station, TX 77845-9547, USA.
- Murray, R.W., Miller, D.J., and Kryc, K.A., 2000. Analysis of major and trace elements in rocks, sediments, and interstitial waters by inductively coupled plasma–atomic emission spectrometry (ICP-AES). *ODP Tech. Note*, 29 [Online]. Available from World Wide Web: <<http://www-odp.tamu.edu/publications/tnotes/tn29/INDEX.HTM>>. [Cited 2003-07-06]
- Nicolas, A., and Ildefonse, B., 1996. Flow mechanisms and viscosity in basaltic magma chambers. *Geophys. Res. Lett.*, 23:2013–2016.
- O’Brien, P.E., Cooper, A.K., Richter, C., et al., 2001. *Proc. ODP, Init. Repts.*, 188 [CD-ROM]. Available from: Ocean Drilling Program, Texas A&M University, College Station TX 77845-9547, USA.
- O’Hanley, D.S., 1996. Serpentinites: records of tectonic and petrological history. *Oxford Monogr. Geol. Geophys.*, 34.
- Puchelt, H., Malpas, J., Falloon, T., Pedersen, R., Eckhardt, J.-D., and Allan, J.F., 1996. *Data report: Ultramafic reference material from Core 147-895D-10W*. In Mével, C., Gillis, K.M., Allan, J.F., and Meyer, P.S. (Eds.), *Proc. ODP, Sci. Results*, 147: College Station, TX (Ocean Drilling Program), 493–496.
- Remaïdi, M., 1993. Etude géochimique de l’association harzburgite, dunite et pyroxénite de l’Arroyo de la Cala (Massif de Ronda, Espagne) [Ph.D. thesis]. Université Montpellier 2, Montpellier, France.
- Rider, M., 1996. *The Geological Interpretation of Well Logs* (2nd ed.): Caithness (Whittles Publishing).
- Robinson, P.T., Von Herzen, R., et al., 1989. *Proc. ODP, Init. Repts.*, 118: College Station, TX (Ocean Drilling Program).
- Schlumberger, 1989. *Log Interpretation Principles/Applications*: Houston (Schlumberger Educ. Services), SMP-7017.
- , 1994. *Log Interpretation Charts: Sugar Land* (Schlumberger), SMP-7006.
- Serra, O., 1984. *Fundamentals of Well-Log Interpretation* (Vol. 1): *The Acquisition of Logging Data*: Dev. Pet. Sci., 15A: Amsterdam (Elsevier).
- , 1986. *Fundamentals of Well-Log Interpretation* (Vol. 2): *The Interpretation of Logging Data*: Dev. Pet. Sci., 15B: Amsterdam (Elsevier).
- , 1989. *Formation MicroScanner Image Interpretation*: Houston (Schlumberger Educ. Services), SMP-7028.
- Shipboard Scientific Party, 1992. Explanatory notes. In Dick, H.J.B., Erzinger, J., Stokking, L.B., et al., *Proc. ODP, Init. Repts.*, 140: College Station, TX (Ocean Drilling Program), 5–33.
- , 1993. Explanatory notes. In Gillis, K., Mével, C., Allan, J., et al., *Proc. ODP, Init. Repts.*, 147: College Station, TX (Ocean Drilling Program), 15–42.
- , 1995. Explanatory notes. In Cannat, M., Karson, J.A., Miller, D.J., et al., *Proc. ODP, Init. Repts.*, 153: College Station, TX (Ocean Drilling Program), 15–42.
- , 1998. Introduction. In Becker, K., Malone, M.J., et al., *Proc. ODP, Init. Repts.*, 174B: College Station, TX (Ocean Drilling Program), 3–9.

- , 1999a. Explanatory notes. *In* Dick, H.J.B., Natland, J.H., Miller, D.J., et al., *Proc. ODP, Init. Repts.*, 176, 1–42 [CD-ROM]. Available from: Ocean Drilling Program, Texas A&M University, College Station, TX 77845-9547, U.S.A.
- , 1999b. Site 735. *In* Dick, H.J.B., Natland, J.H., Miller, D.J., et al., *Proc. ODP, Init. Repts.*, 176, 1–314 [CD-ROM]. Available from: Ocean Drilling Program, Texas A&M University, College Station, TX 77845-9547, U.S.A.
- , 2001. Explanatory notes. *In* Christie, D.M., Pedersen, R.B., Miller, D.J., et al., *Proc. ODP, Init. Repts.*, 187, 1–42 [Online]. Available from World Wide Web: <http://www-odp.tamu.edu/publications/187_IR/VOLUME/CHAPTERS/IR187_02.PDF>. [Cited 2003-07-06]
- , 2002. Explanatory notes. *In* Tarduno, J.A., Duncan, R.A., Scholl, D.W., et al., *Proc. ODP, Init. Repts.*, 197 [Online]. Available from World Wide Web: <http://www-odp.tamu.edu/publications/197_IR/chap_02/chap_02.htm>. [Cited 2003-07-06]
- Shipley, T.H., Ogawa, Y., Blum, P., et al., 1995. *Proc. ODP, Init. Repts.*, 156: College Station, TX (Ocean Drilling Program).
- Sims, K.W., Gladney, E.S., Lundstrom, C., and Bower, N.W., 1988. Elemental concentrations in Japanese silicate rock standards: a comparison with the literature. *Geostand. Newsl.*, 12:379–389.
- Smith, D.C., Spivack, A.J., Fisk, M.R., Haveman, S.A., Staudigel, H., and ODP Leg 185 Shipboard Scientific Party, 2000. Methods for quantifying potential microbial contamination during deep ocean coring. *ODP Tech. Note*, 28 [Online]. Available from World Wide Web: <<http://www-odp.tamu.edu/publications/tnotes/tn28/INDEX.HTM>>. [Cited 2003-07-06]
- Sparks, J.W., and Zuleger, E., 1995. Data report: Chemical analyses of the Leg 140 reference sample. *In* Erzinger, J., Becker, K., Dick, H.J.B., Stokking, L.B. (Eds.), *Proc. ODP, Sci. Results*, 137/140: College Station, TX (Ocean Drilling Program), 353–355.
- Streckeisen, A., 1974. Classification and nomenclature of plutonic rocks. *Geol. Rundsch.*, 63:773–786.
- Tommasi, A., Gibert, B., Seipold, U., and Mainprice, D., 2002. Anisotropy of thermal diffusivity in the upper mantle. *Nature*, 411:783–786.
- Tréhu, A.M., Bohrmann, G., Rack, F.R., Torres, M.E., et al., 2003. *Proc. ODP, Init. Repts.*, 204 [CD-ROM]. Available from: Ocean Drilling Program, Texas A&M University, College Station TX 77845-9547, USA.
- United States Geological Survey, 2003. U.S. Geological Survey geochemical reference materials and certificates [Online]. Available from World Wide Web: <http://minerals.cr.usgs.gov/geo_chem_stand>. [Cited 2003-07-06]
- Vacquier, V., 1985. The measurement of thermal conductivity of solids with a transient linear heat source on the plane surface of a poorly conducting body. *Earth Planet. Sci. Lett.*, 74:275–279.

Figure F1. Illustration of ODP labeling scheme used for holes, cores, and sections.

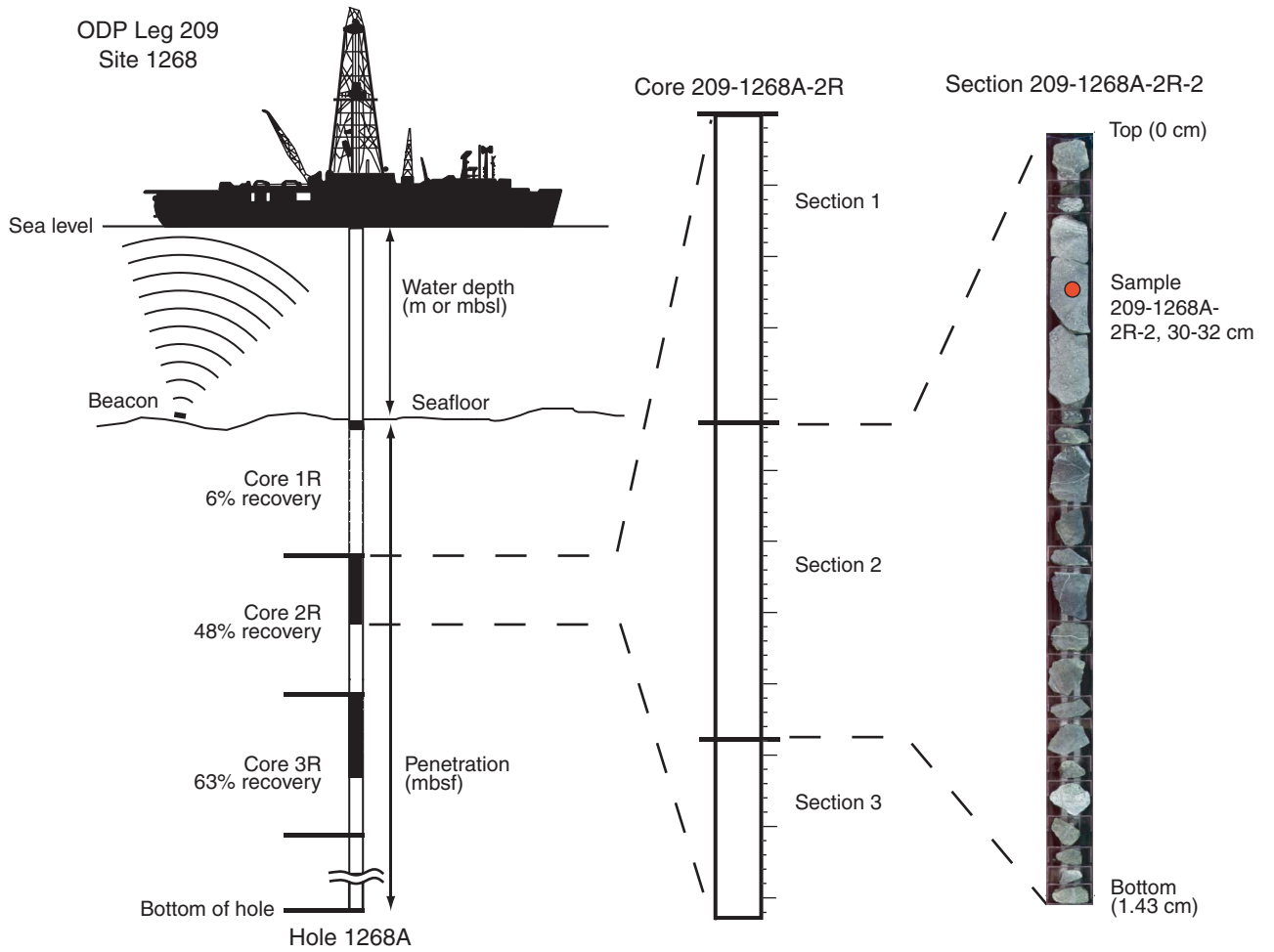
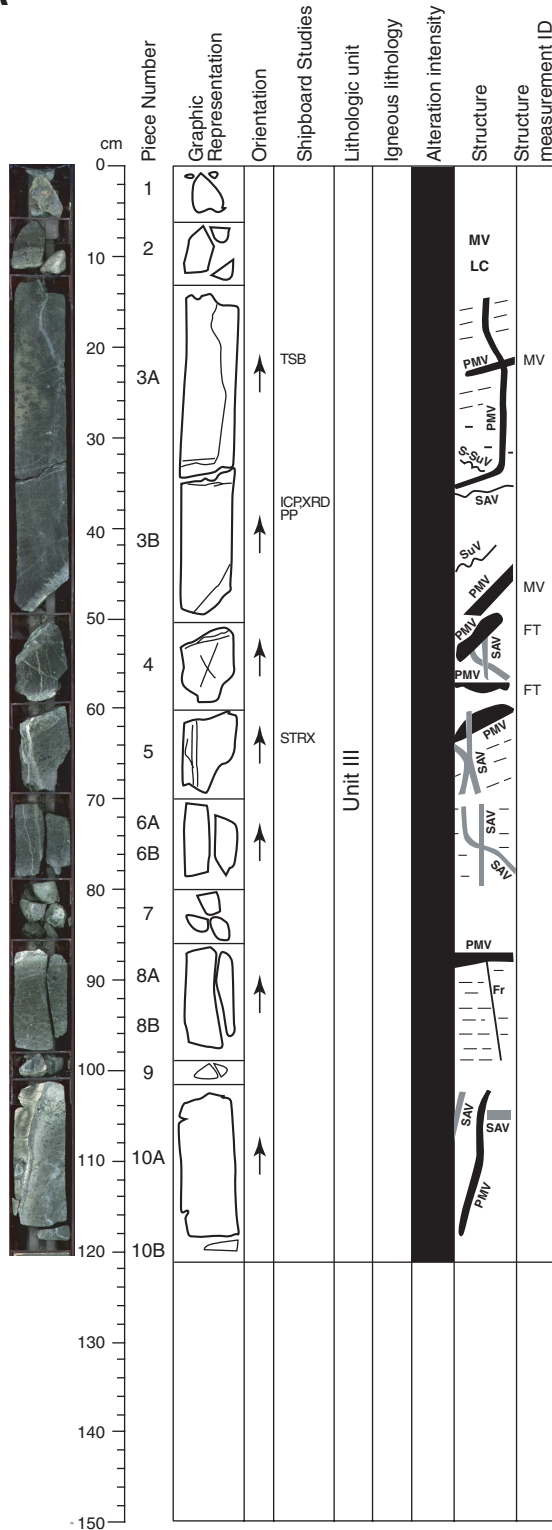


Figure F2. A. Example of a visual core description (VCD) log sheet. Data summarized include not only the igneous observations but those of other groups as well. (Continued on next page.)

A



209-1268A-16R-1 (Section top: 82.40 mbsf)

UNIT-III: Harzburgite/Dunite

Pieces 1–10

COLOR: Green in serpentinized harzburgite. Gray in talc altered gabbroic dikelets.

PRIMARY MINERALOGY:

Olivine	Mode 82%
Orthopyroxene	Mode 18%
	Size 3–10 mm
	Shape/Habit Anhedral
Spinel	Mode 1%

COMMENTS: This section consists of serpentinized harzburgite with porphyroclastic texture. Gabbroic segregations characterized by large spinel grains are present at 24 cm and 109 cm. A gabbroic dike cuts the sequence at 50 cm. Locally, mylonitic bands are associated with dikelets and segregations.

SECONDARY MINERALOGY:

COMMENTS: This section consists of green, completely serpentinized harzburgite (SHz) with local occurrences of crosscutting, completely chlorite-talc altered gabbroic dikelets (Pieces 3, 4, 8, and 10). Typically these dikelets have black and green alteration halos. Late serpentine veins cut across and splice the dikelets. The lower part of Piece 2 is a completely altered pyroxenite.

VEIN ALTERATION: This section contains three generations of veins. An earlier generation of wispy serpentine veins is well developed in the green serpentinized harzburgite (SHz). This generation cuts across magmatic features and offsets them (e.g., Piece 3A). Associated with this generation are also massive pyrite-iron oxide veinlets. Perpendicular thick serpentine-talc veins crosscut these two generations of veins. These veins run parallel to the gabbro layer. Thicker gabbroic veins display cross-fracture of chrysotile-talc veins.

THIN SECTIONS: 1268A-16R-1 21-24cm

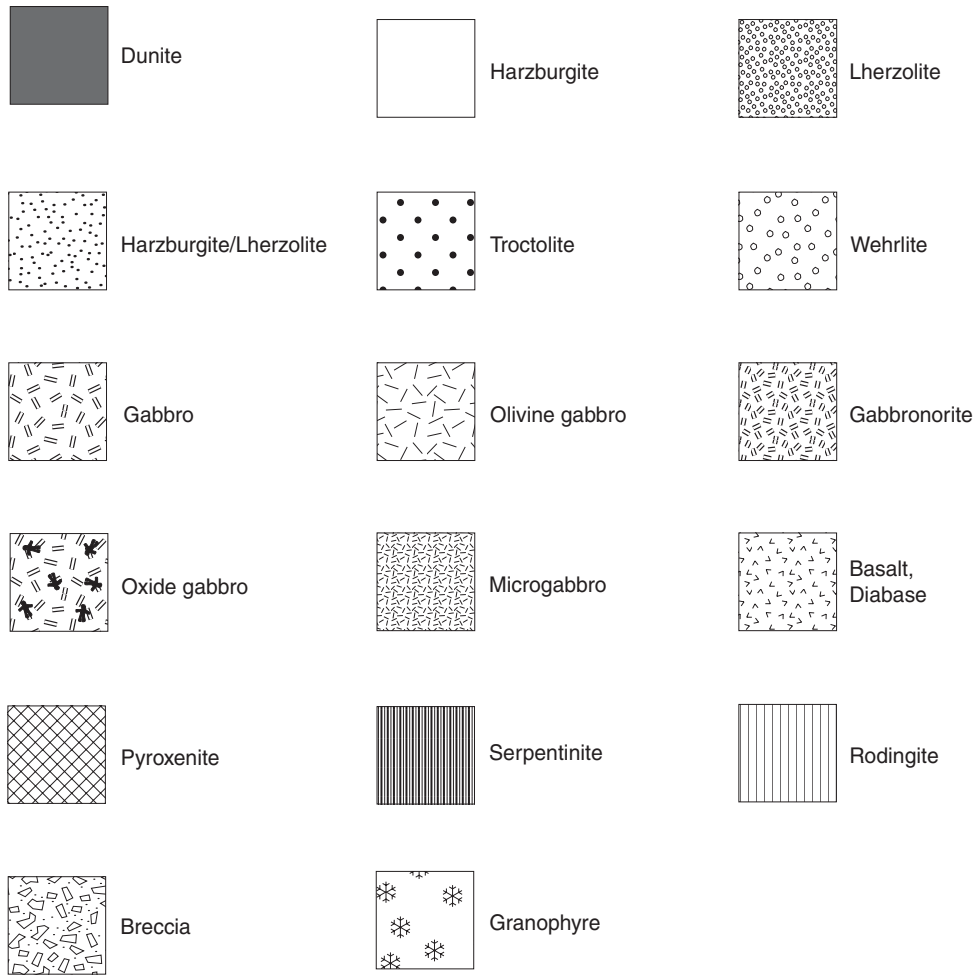
STRUCTURE:

The section is characterized by weakly foliated porphyroclastic serpentinized harzburgite. The crystal-plastic foliation has a nearly horizontal trace in core cut face. Pieces 2–4, 6, 8, and 10 are cut by a altered pyroxenitic magmatic veins (PMV) and Piece 8 is cut by an altered pyroxenitic-gabbroic composite vein (CMV). Darker to light green serpentine alteration veins (SAV1) or tension gashes cut the PMV perpendicular to its vein wall. The gashes are widest in the center of the vein and taper and terminate in the serpentinized harzburgite accommodating volume expansion in the altered olivine-rich rock. Prominent white and light green non-differentiated serpentine/talc veins (SAV2) in turn cut the MV, the orthogonal tension gashes and each other. Sulfide veins (SuV) appear to cut many of the SAV2 or earlier veins. All magmatic and alteration veins are post-kinematic with respect to the crystal-plastic deformation. Crosscutting relationships demonstrate that CP>MV>SAV1>SAV2>SuV.

Figure F2 (continued). B. Symbols used in VCDs.

B

Igneous rock types for lithology column



Alteration intensity

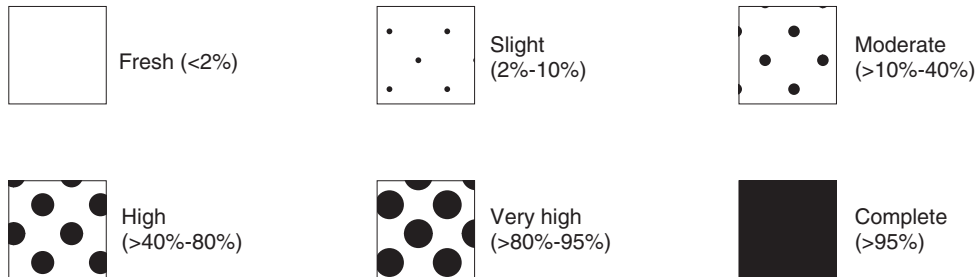


Figure F3. Modal classification scheme for plutonic igneous rocks, after Streckeisen (1974).

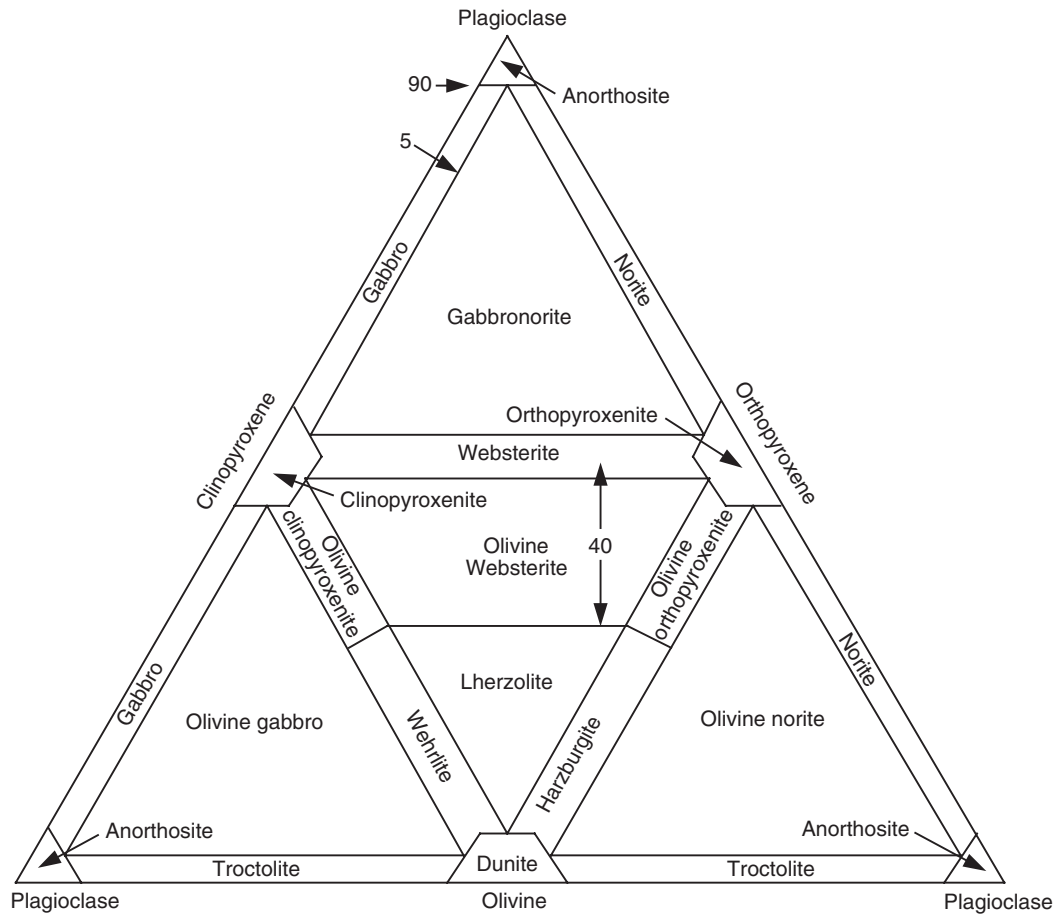
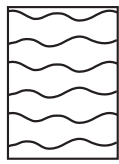


Figure F4. Criteria and number scheme used to describe metamorphic veins.

Vein type

Paragranular: following grain boundaries

Transgranular: dissecting grain boundaries



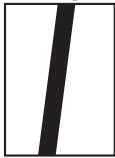
1



2

Vein shape

Straight



1

Kinked



2

Sigmoidal



3

Irregular



4

Vein connectivity

Single



1

Nonbranched



2

Occasionally branched



3

Branched



4

Network



5

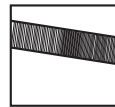
Vein texture

Massive



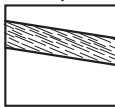
1

Cross fiber



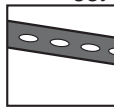
2

Slip fiber



3

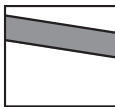
Vuggy



4

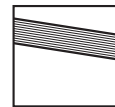
Vein structure

Uniform



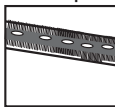
1

Banded



2

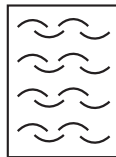
Composite



3

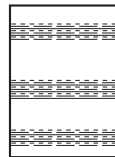
Particular vein geometries:

En echelon



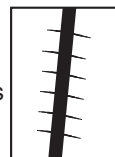
1

Ribbon



2

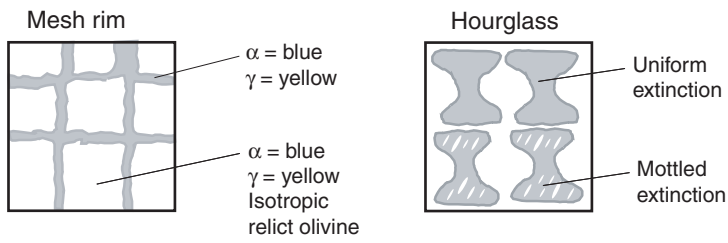
Cross fractures



3

Figure F5. Schematic sketches of different serpentinite microtextures (see text and Table T3, p. 61, for details).

Pseudomorphic texture



Nonpseudomorphic texture

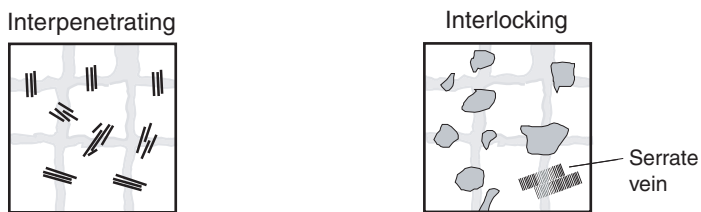


Figure F6. Intensity scales used for structural identification. See text for detailed explanation.














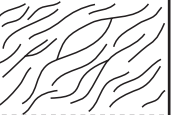





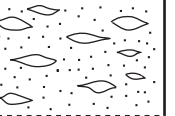


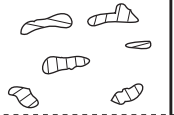


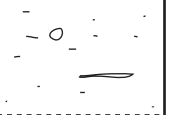


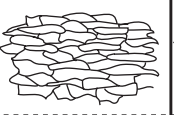


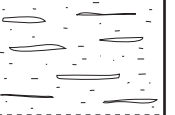
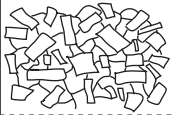



Feature	0	1	2	3	4	5
Joints/ Open fractures	 No open fractures	 <1 per 10 cm	 1-5 per 10 cm	 >5 per 10 cm		
Veins	 No veins	 <1 per 10 cm	 1-5 per 10 cm	 5-10 per 10 cm	 10-20 per 10 cm	 >20 per 10 cm
Serpentine foliation	 Massive	 Weakly foliated	 Moderately foliated	 Strongly foliated		
Cataclastic deformation	 Undeformed	 Minor fracturing No sig. grain size reduction	 Moderate fracturing No sig. grain size reduction	 Dense anastomosing fracturing and incipient brecciation (<20% matrix)	 Well-developed fault brecciation; clast rotation (20% - 70% matrix)	 Cataclasite (>70% matrix)
Peridotite crystal-plastic deformation	 Undeformed protogranular	 Porphyroclastic weakly foliated	 Porphyroclastic strongly foliated	 Porphyroclastic (Protomylonite)	 Mylonite	 Ultramylonite
Gabbro crystal-plastic deformation	 Undeformed	 Weakly foliated	 Strongly foliated	 Porphyroclastic (Protomylonite)	 Mylonite	 Ultramylonite
Magmatic foliation	 Isotropic: no shape fabric	 Weak shape fabric	 Moderate shape fabric	 Strong shape fabric		

Figure F7. Core reference frame used for orienting structures. A. Cut face. B. Three-dimensional perspective of core.

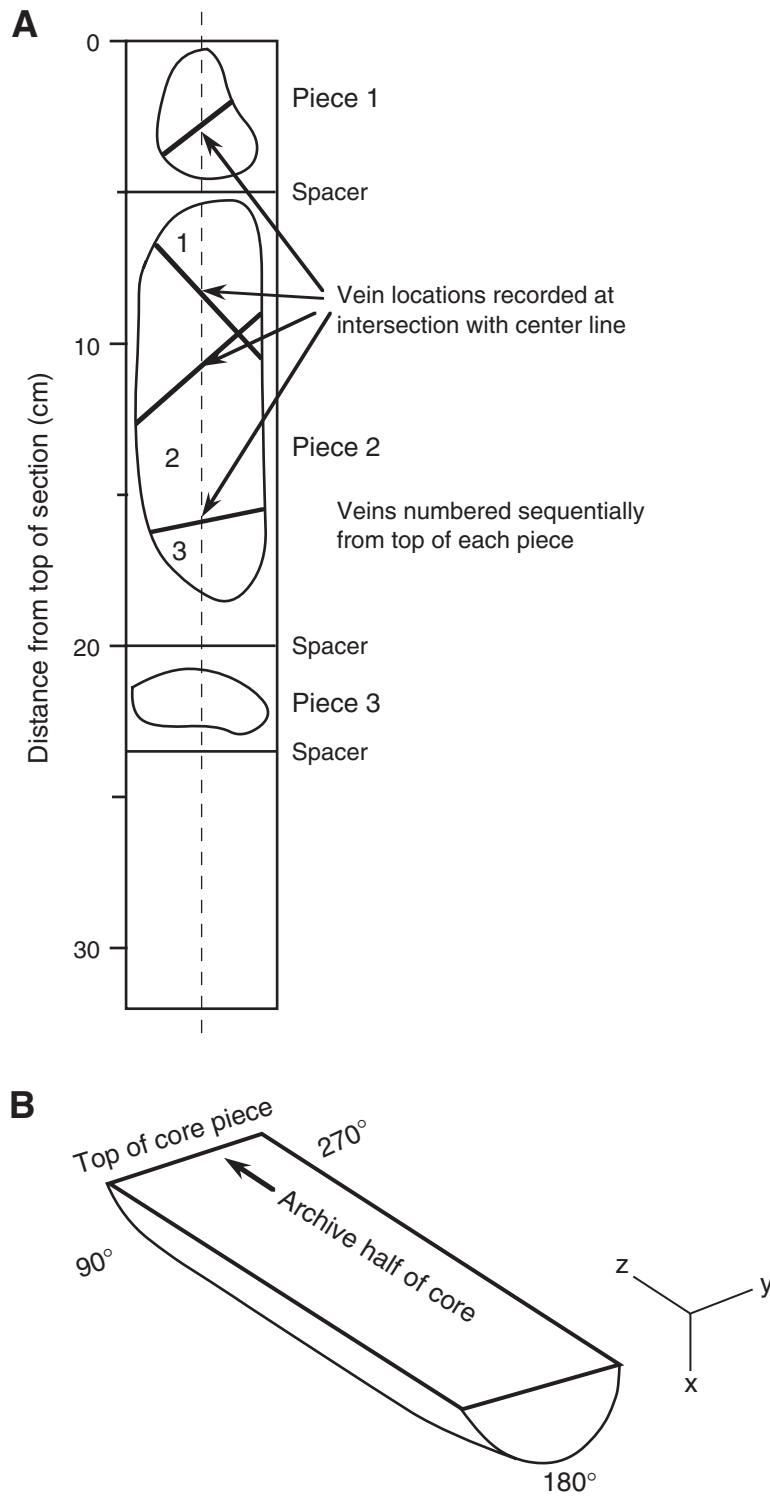
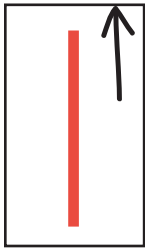
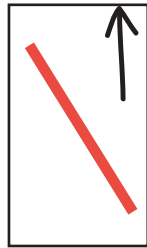


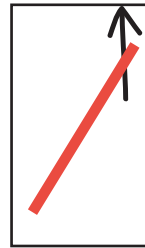
Figure F8. Convention notation (0, 1, or 2) used for the orientation of the needle probe in thermal conductivity measurement data tables. The arrow points to the top of the core.



0 - parallel
to core axis



1 - oblique
to core axis



2 - oblique
to core axis

Figure F9. ODP orientation convention for paleomagnetic samples.

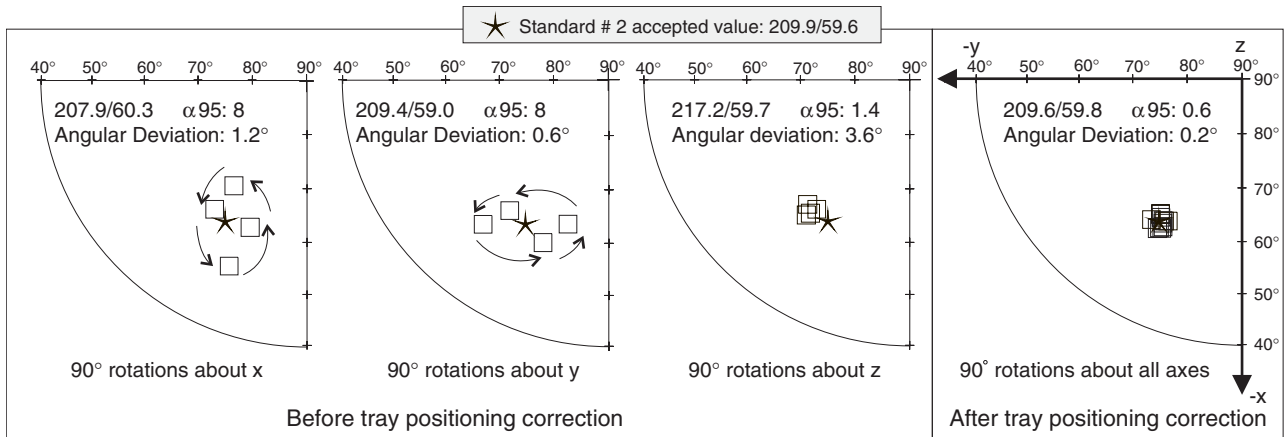


Figure F10. Equal-area projections illustrating the reduction of scatter after repositioning the discrete sample tray. Left-hand plots show results for standard #2 when rotated at 90° intervals about the magnetometer x-, y-, and z-axes, respectively. Note the higher scatter but lower angular deviation of individual directions for rotations about the x- or y-axis. Right-hand plot shows results for the same sample positions after realignment of the discrete sample tray.

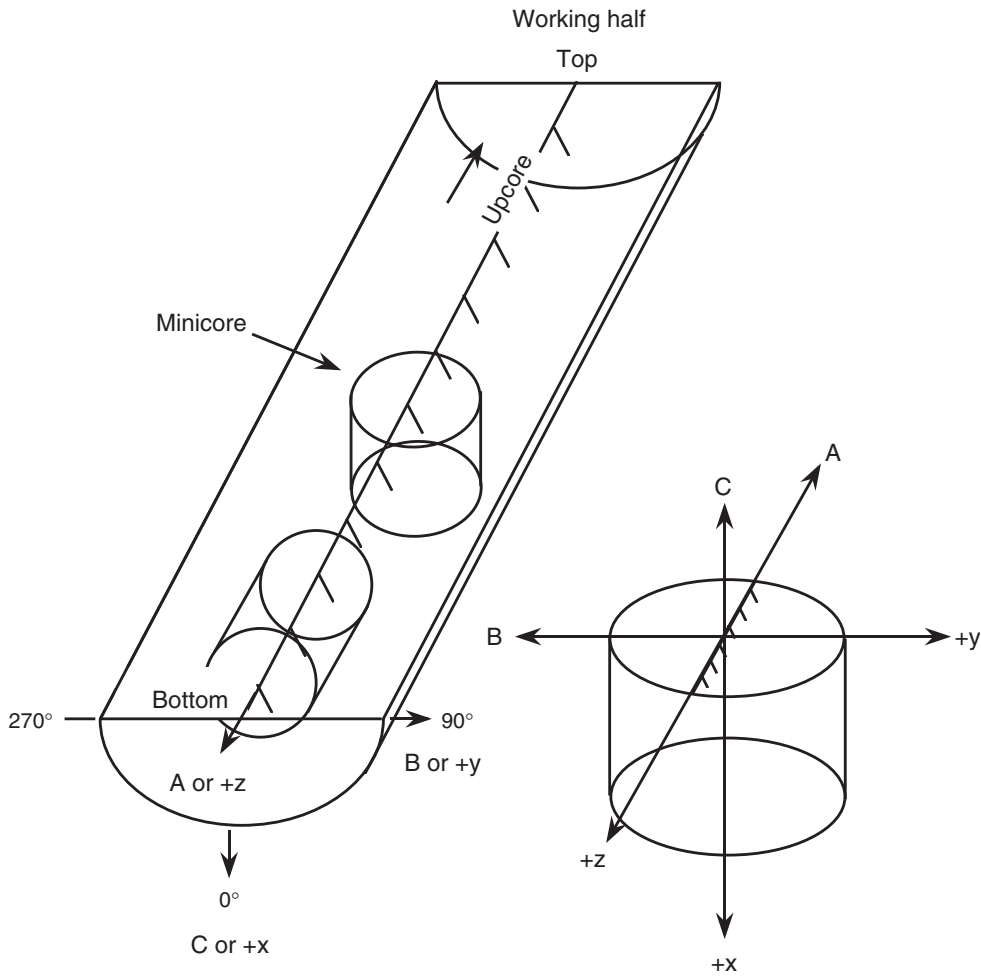


Figure F11. Baseline values for classifying SeaWiFS images using Ulead Photo Impact image tone mapper.

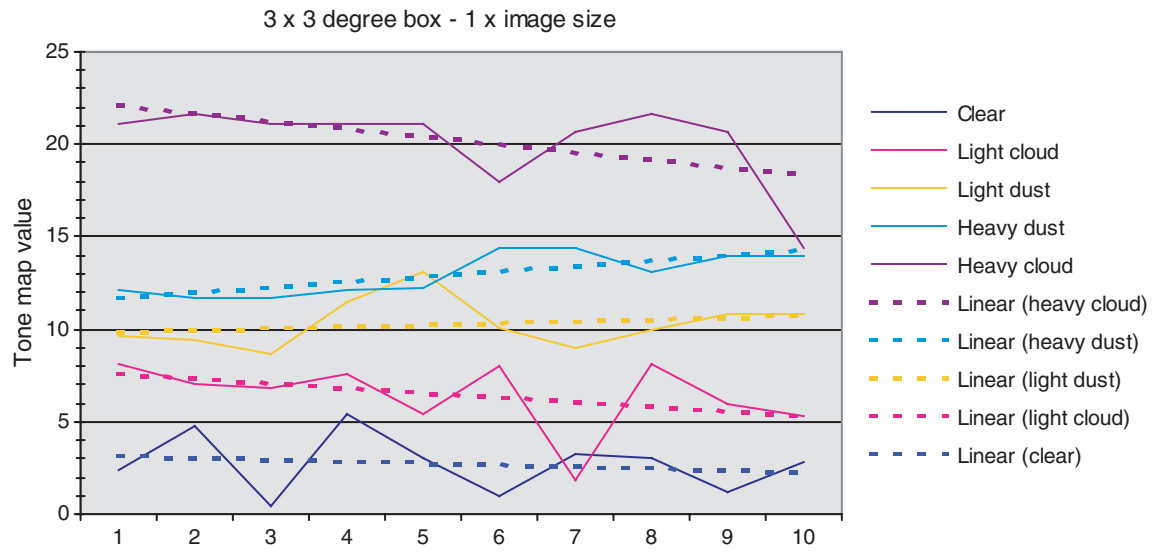


Figure F12. Portable membrane filtration apparatus for atmospheric microbiology culture-based studies.



Figure F13. Portable liquid impinger for atmospheric collection of microorganisms for molecular and transmission electron microscopy analysis.



Figure F14. Air sampler for analysis of metals and organic pollutants.

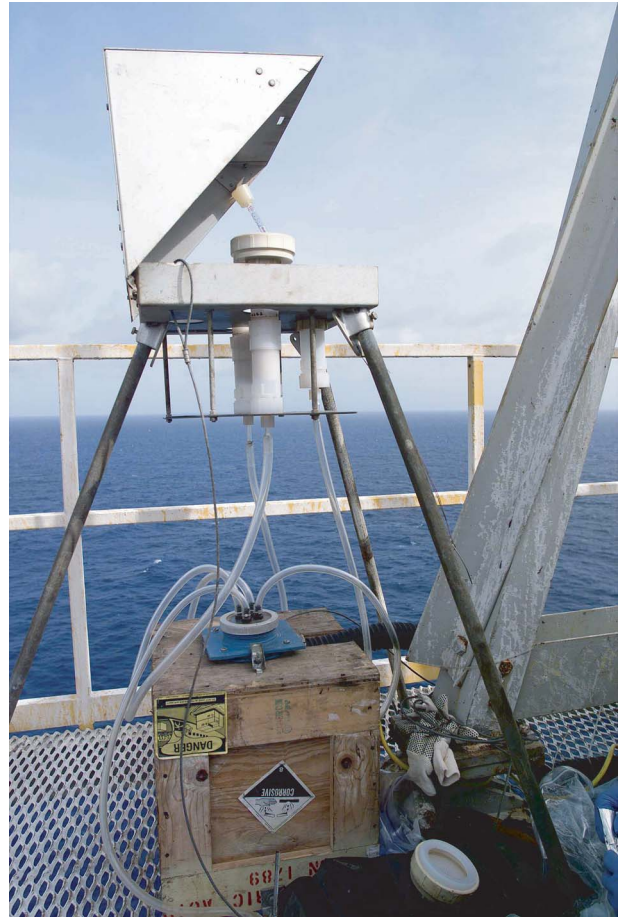


Figure F15. Configuration of the wireline tool strings. See Tables T11, p. 73, and T12, p. 74, for tool specifications and measurements.

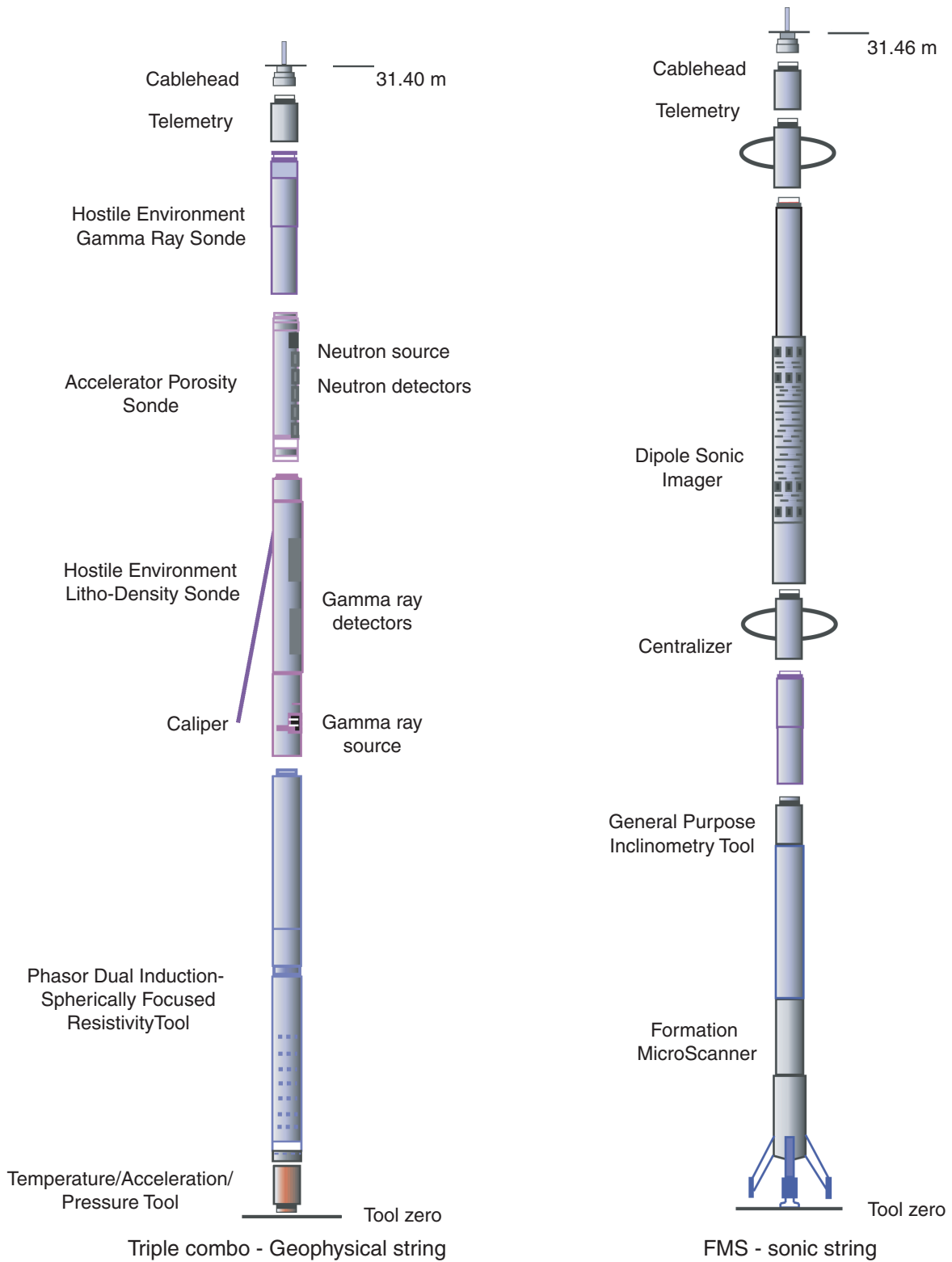


Figure F16. Configuration of the RAB-8 tool. OD = outer diameter, ID = inner diameter.

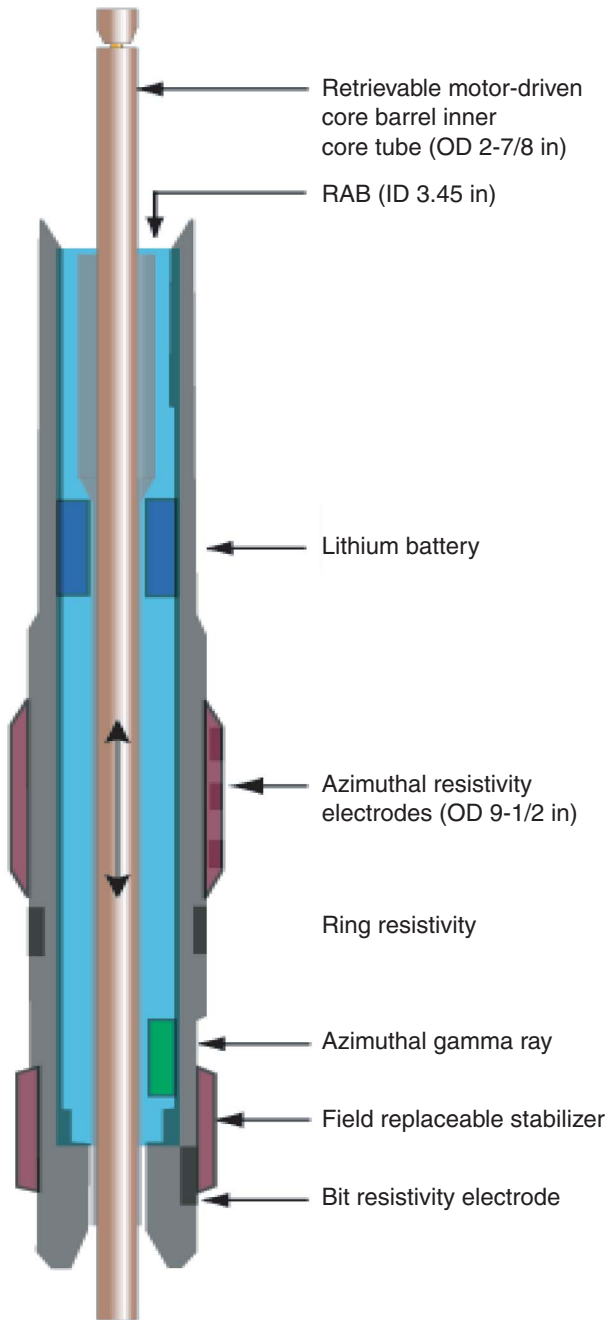


Table T1. Glossary of metamorphic petrology terms.

Term	Definition
Apparent fibers	Cross sections of serpentine plates that look fibrous in thin section.
Asbestiform	Crystals (chrysotile, tremolite) are thin hairlike fibers that are mechanically separable.
Background alteration	Alteration has pervasively affected the entire rock and is not primarily bound to veins or foliation planes.
Banded vein	Vein with rhythmic layering parallel to the vein walls.
Bastite	Serpentine texture after chain and layer silicates preserving important features of the protolith (e.g., plastic deformation) and pre-serpentine alteration assemblages.
Brucite(?)	Brucite was tentatively identified by anomalous cream-brown interference colors, by yellow color in plane polarized light (if weathered), and by shape (more bladed or prismatic than serpentine).
Chrysotile	White asbestiform serpentine, usually in veins with magnetite; most common in paragonular veins.
Composite vein	Compositionally zoned vein containing different mineral assemblages that may or may not represent different generations.
Cross-fiber vein	Asbestiform or pseudofibrous vein in which the fibers (or apparent fibers) are oriented perpendicular to the vein walls.
Fibrous	Single crystals resembling organic fibers or crystalline aggregates that look like they are composed of fibers. If fibers are mechanically separable (e.g., by probing the sample with a needle), they are asbestiform. If they are not separable, they are pseudofibrous. If the fibers have the normal strength and brittleness of the mineral, they are acicular.
Hourglass texture	Similar to mesh texture, but a distinction between mesh rim and mesh center is not possible. This texture is related to fractures in the mineral grains of the protolith and is hence not strictly a pseudomorph texture.
Interlocking texture	More or less equant serpentine grains and/or serrate serpentine veins replace pseudomorph serpentine.
Interpenetrating texture	Elongate, interpenetrating blades of γ -serpentine replace pseudomorph serpentine.
Massive vein	Veins that are homogeneous and completely filled.
Mesh texture	Pseudomorph texture resembling a fisherman's net. The mesh rim represents the cord of the net and the mesh centers represent the empty areas between the cords of the net. The outer edge of a mesh cell coincides either with the edge of a mineral grain or with a fracture within the mineral grain of the protolith.
Nonpseudomorph texture	Does not preserve the texture of the protolith. Can only be recognized under cross polarized light. Includes interpenetrating and interlocking textures.
Paragonular vein	Anastomosing vein or vein network that is foliation parallel and wraps around porphyroclasts.
Patch	Polycrystalline domain, more or less isolated and surrounded by host rock, that is compositionally distinct from the host rock. Patches can be secondary features (i.e., as a consequence of patchy alteration) or primary igneous features where the differences may have been enhanced by alteration.
Picrolite	Vein-filling serpentine that is white, cream color, pale yellow, to apple green in color and may be either massive or pseudofibrous in habit. Picrolite can be either lizardite, chrysotile, or antigorite. Picrolite veins are usually transgranular.
Pseudofibrous	Crystals or crystalline aggregates that have fibrous appearance but are not composed of separable fibers.
Pseudomorph texture	Preserves the texture of the protolith. Includes mesh and hourglass textures. Can be recognized in plane polarized light.
Ribbon texture	Special form of transitional texture. Mesh rims extend over several grains of the protolith, creating a set of irregular bands.
Rodingite	A calcium metasomatized rock in which the primary igneous composition and texture have been destroyed to an extent that the nature of the protolith is uncertain. If the nature of the protolith can be discerned but calcium metasomatism is obvious, the rock was described as rodingitized.
Selvages	Wallrock along a vein that is completely altered to secondary minerals and has a sharp contact to the host rock.
Slip-fiber vein	Asbestiform or pseudofibrous vein in which the fibers (or apparent fibers) are oriented more or less parallel to the vein walls.
Transgranular vein	Vein or vein network at any angle to the foliation planes that crosscut porphyroclasts and/or other large crystals.
Transitional texture	Preserves some of the texture of the protolith. May appear pseudomorph in plane polarized light but without mesh or hourglass texture in cross polarized light. Includes mesh textures with isotropic mesh centers and ribbon textures.
Type 1 hourglass texture	Extinction sweeps continuously across mesh center.
Type 2 hourglass texture	Recrystallization of serpentine has produced a mottled extinction pattern.
Vein halos	Zones (millimeter to centimeter wide) along a vein in which the rock is more intensely altered, or altered in a different style, than the host rock. A halo can have a sharp or diffuse contact to the host rock.
Vuggy vein	Incompletely filled vein.
α -Serpentine mesh-rim texture	Rims of mesh cells are length-fast.
α -Serpentine	Length-fast fibers.
γ -Serpentine mesh-rim texture	Rims of mesh cells are length-slow.
γ -Serpentine	Length-slow fibers.

Table T2. List of mineral acronyms.

Minerals*	
OI	Olivine
Opx	Orthopyroxene
Cpx	Clinopyroxene
Spi	Spinel
Amph	Amphibole
Liz	Lizardite
Ant	Antigorite
Chry	Chrysotile
Srp	Serpentine (group)
Brc	Brucite
Trm	Tremolite
Act	Actinolite
Ath	Anthophyllite
Cum	Cummingtonite
Chl	Chlorite
Tlc	Talc
Mt	Magnetite
Sulf	Sulfides
Carb	Carbonates
Zeo	Zeolite (group)
Plag	Plagioclase
Preh	Prehnite
Qtz	Quartz
Ep	Epidote

Note: * = after Kretz, 1983.

Table T3. Key for preliminary serpentine identification.

Texture	α -Serpentine	γ -Serpentine
Mesh rim	Liz	Liz Chry Ant
Hourglass	Liz	Chry Ant
Interpenetrating	NA	Chry + brc Ant
Interlocking	Liz	Liz Chry Ant
Serrate veins	Liz	Chry

Notes: Serpentine identification is based on microbeam refraction experiments (O'Hanley, 1996, pp. 62–65). NA = not applicable.

Table T4. Checklist used for spreadsheet comments associated with each structural identifier. (See table notes. Continued on next page.)

Structural identifier	Observations included
Subhorizontal microcracks (Shm)	Drilling-induced fractures
Joints (J)	Joint density Orientation Plume structures on joint surface
Veins (V)	Orientation of veins and vein-array boundaries Width and length Magnitude and nature of offset: n = normal, r = reverse, ss = strike slip Density of vein network (N/10 cm) Array characteristics Sense of shear: d = dextral, s = sinistral Angle between new vein segments and array boundary (measure of array dilatation) Internal structure of fibers Crack-seal structures and number of vein-opening events Wallrock alteration and shape ~ sharp or diffuse boundaries Vein terminations (splayed or tapered) Vein mineralogy
Faults (F)	Fault-zone thickness, orientation, and density Movement sense: r = reverse, n = normal, d = dextral, s = sinistral Movement offset (displacement, millimeters) Intensity of cataclastic fabric (Cf) Matrix material (gouge or secondary minerals) Overprinting of preexisting fabric Semibrittle
Breccias (B)	Hydrothermal (Bh), magmatic (Bm), or cataclastic (Bc) Clast size and shape, matrix composition, relative proportions
Cleavages (C)	Style of cleavage (e.g., crenulation [Cc], spaced [Cs]) Spacing or wavelength Angle between cleavage and earlier fabrics, noting directions of larger-scale fold closures
Folds (Fo)	Inter-limb angle Estimate of hinge curvature (e.g., kink, round) Asymmetry of hingeline relative to other fabrics (e.g., stretching lineations, etc.) Other geometrical aspects preserved in core (e.g., wavelength, amplitude, etc.) Number of folds, if >1
Serpentinization foliation	Strength of foliation Orientation of foliation in core reference frame
Crystal-plastic fabrics (Cpf)	Intensity of fabric Intensity of fabric in retrograde assemblage Orientation of foliation (Sp) and lineation (Lp) L-, LS-, and S-tectonite Shear sense indicators: block-rotated porphyroclasts, asymmetric augen, SC fabrics, discrete shear bands, mica-fish, and tension gash arrays: r = reverse, n = normal, d = dextral, s = sinistral Mineralogical segregation or banding
Magmatic fabrics (Mf)	Intensity and orientation of foliations (Sm) and lineations (Lm) Minerals that define the shape and/or crystallographic preferred orientations Angle between crystallographic and shape fabrics Orientation of subfabrics
Compositional layering (Cl)/ gradational boundaries (Gb)	Type of layering (e.g., sedimentary, igneous cumulate, alteration, etc.); orientation, thickness, and density of layers
Igneous contacts (Ic)	Orientation and density Concordant or discordant

Table T4 (continued).

Structural identifier	Observations included
Crosscutting relationships	Intrusive relationships, relative chronology of the different fabrics Angle between compositional layering and magmatic or crystal-plastic fabric

Notes: This checklist notes structural characteristics that were searched for in macroscopic core samples. These characteristics supplement the information required by the spreadsheet and were noted in the comments section of the spreadsheet. The abbreviations for these features were used to document crosscutting relationships (where > indicates "older than") on the structure section of the visual core descriptions.

Table T5. Microstructure of gabbroic rocks.

Textural group	Plagioclase	Olivine	Pyroxene	Physical state
1	No or minor crystal-plastic deformation microstructures (e.g., deformation twins, undulose extinction)	No deformation microstructures \pm local undulose extinction and/or local subgrain development	No deformation microstructures	Primarily magmatic
a	Random shape orientation			
b	Preferred shape orientation			
2	<30% fine-grained recrystallized matrix; deformation twins and subgrain boundaries may be present	Common subgrain boundaries and undulose extinction	No deformation microstructures \pm minor crystal-plastic deformation microstructures	Crystal-plastic \pm magmatic
3	>30% recrystallized matrix; deformation twins, subgrain boundaries, and undulose extinction common; moderate shape preferred orientation; strong crystallographic preferred orientation	Elongated aggregates of neoblasts	Kinked grains; common to extensive recrystallization	Crystal-plastic
4	Strongly bimodal grain size distribution; localized fine-grained neoblasts, polygonal neoblasts, sutured neoblasts	Closely spaced subgrain boundaries; pervasive undulose extinction extensive neoblasts	Bent/kinked porphyroclasts; localized recrystallization	Crystal-plastic
5	Common intracrystalline microfractures associated with very fine-grained neoblasts; extensive kinked and deformation twinned grains; pervasive undulose extinction; may contain hydrothermal alteration mineral assemblages	Same as plagioclase	Same as plagioclase	Semibrittle
6	Intra/intercrystalline microfractures and cataclastic bands; extensive kinked and deformation twinned grains; pervasive undulose extinction	Same as plagioclase	Same as plagioclase	Brittle/cataclastic

Table T6. Analytical conditions for ICP-AES analyses.

Element	Wavelength (nm)	Integration time/calculation point (s)	Photomultiplier voltage	Photomultiplier gain	Increment between points (nm)	Calculation points (N)	Limit of detection (ppm)
Al*	396.152	1.0	720	1	0.0027	5	0.03
Ba	455.403	1.0	730	10	0.0027	5	39
Ca*	393.366	1.0	350	1	0.0027	5	0.06
Co	228.616	1.0	990	100	0.0027	5	32
Cr	267.716	1.0	860	100	0.0027	5	41
Cu	324.754	1.0	690	10	0.0027	5	2
Fe*	259.940	1.0	560	10	0.0027	5	0.13
K*	766.490	1.0	990	100	0.0027	5	0.01
Mg*	285.213	1.0	600	10	0.0027	5	0.41
Mn*	257.610	1.0	580	100	0.0027	5	0.001
Na*	589.592	1.0	610	10	0.0027	5	0.03
Ni	231.604	1.0	990	100	0.0027	5	165
P	178.229	1.0	933		0.0027	5	0.06†
Si*	251.611	1.0	570	10	0.0027	5	0.22
Sr	407.771	1.0	560	10	0.0027	5	5
V	292.402	1.0	960	100	0.0027	5	5
Y	371.029	1.0	620	100	0.0027	5	2
Zr	343.823	1.0	640	100	0.0027	5	2
Ti*	334.941	1.0	570	10	0.0027	5	0.01
Sc	361.384	1.0	660	100	0.0027	5	0.4

Notes: ICP-AES = inductively coupled plasma–atomic emission spectrometry. N = number. * = limit of detection reported as oxide (wt%). † = from Shipboard Scientific Party, 2002 (Leg 197). Instrument detection limits represent 3 times the instrument blank. This table is also available in [ASCII](#).

Table T7. Estimates of accuracy and precision for JY2000 ICP-AES major and trace element analyses. (See table notes. Continued on next three pages.)

Standard	Date (2003)	Major element oxide (wt%)										Total	
		SiO ₂	TiO ₂	Al ₂ O ₃	Fe ₂ O ₃	MgO	MnO	CaO	Na ₂ O	K ₂ O	P ₂ O ₅		
ROA-3*	15 May	48.93	0.71	8.33	8.85	25.68	0.15	7.61	0.83	<0.01		101.09	
	15 May	47.80	0.72	8.39	8.85	25.44	0.15	7.86	0.85	<0.01		100.06	
	26 May	48.37	0.68	8.08	8.42	24.53	0.15	7.55	0.81	0.01	0.03	98.63	
	30 May	46.00	0.72	8.33	8.84	26.41	0.16	7.73	0.84	<0.01		99.03	
	30 May	44.95	0.69	8.12	8.46	25.08	0.15	7.58	0.82	<0.01		95.85	
	1 Jun	46.49	0.68	8.27	8.65	26.82	0.16	7.75	0.83	<0.01		99.65	
	4 Jun	45.52	0.70	8.01	8.66	25.21	0.16	7.85	0.86	<0.01		96.97	
	7 Jun	48.68	0.70	8.14	8.65	25.36	0.16	7.79	0.85	<0.01		100.33	
	9 Jun	48.01	0.68	8.25	8.77	24.95	0.16	7.80	0.87	0.01		99.50	
	13 Jun	47.48	0.69	8.07	8.52	25.57	0.16	7.70	0.89	0.01		99.09	
	14 Jun	45.86	0.70	8.37	8.05	25.46	0.15	7.70	0.88	<0.01		97.17	
	21 Jun	47.01	0.71	8.23	8.82	25.61	0.15	7.78	0.85	<0.01		99.16	
	Average (wt%):		47.09	0.70	8.22	8.63	25.51	0.16	7.73	0.85	0.01		
	Preferred values (wt%):		49.08	0.72	7.89	8.67	24.59	0.15	7.55	0.84	<0.02		
	Standard deviation (wt%):		1.32	0.01	0.13	0.24	0.15	0.005	0.10	0.02	0.00		
	Precision (%):		2.80	1.43	1.58	2.78	0.59	3.13	1.29	2.35			
Accuracy (%):		-4.23	-2.86	4.01	-0.46	3.61	6.25	2.33	1.18				
JP-1	15 May	44.76	<0.01	0.59	8.50	45.69	0.12	0.55	<0.03	<0.01		100.21	
	30 May	44.48	<0.01	0.68	8.46	46.86	0.12	0.62	0.03	0.01		101.26	
	30 May	44.32	<0.01	0.69	8.65	47.30	0.12	0.64	0.03	0.01		101.76	
	1 Jun	43.66	<0.01	0.54	8.14	46.33	0.12	0.47	<0.03	<0.01		99.27	
	1 Jun	43.12	<0.01	0.55	8.15	45.66	0.12	0.46	<0.03	<0.01		98.06	
	4 Jun	43.70	0.01	0.63	8.31	46.83	0.12	0.57	0.03	<0.01		100.20	
	4 Jun	41.98	0.01	0.82	8.43	44.38	0.12	0.59	0.03	0.01		96.37	
	7 Jun	43.68	0.01	0.67	8.54	45.91	0.12	0.58	0.03	0.01		99.55	
	7 Jun	44.47	0.01	0.65	8.59	45.11	0.12	0.60	<0.03	0.01		99.56	
	9 Jun	44.41	0.01	0.67	8.62	46.35	0.12	0.59	<0.03	<0.01		100.77	
	9 Jun	42.55	0.01	0.67	8.37	44.79	0.12	0.60	<0.03	<0.01		97.11	
	13 Jun	44.23	0.01	0.66	8.15	44.39	0.12	0.62	<0.03	0.01		98.18	
	13 Jun	43.62	0.01	0.66	8.58	46.28	0.12	0.59	<0.03	<0.01		99.86	
	14 Jun	41.87	0.02	0.65	8.03	44.89	0.11	0.59	<0.03	0.01		96.16	
	14 Jun	41.92	0.01	0.66	8.03	46.05	0.12	0.58	0.03	<0.01		97.40	
	21 Jun	43.21	0.01	0.66	8.69	46.12	0.12	0.63	0.03	0.01		99.47	
21 Jun	42.81	0.01	0.66	8.49	45.85	0.12	0.62	<0.03	<0.01		98.56		
Average (wt%):		43.46	0.01	0.65	8.40	45.81	0.12	0.58	0.03	0.01			
Preferred values (wt%):		42.39		0.62	8.34	44.72	0.12	0.56	0.02	<0.01			
Standard deviation (wt%):		0.96	0.003	0.06	0.22	0.86	0.002	0.05	0.01	0.00			
Precision (%):		2.21	30.00	9.23	2.62	1.88	1.67	8.62	63.14				
Accuracy (%):		2.46		4.62	0.71	2.38		3.45	33.33				
DTS-1	26 May	36.17	<0.01	0.20	7.92	43.70	0.11	0.09	<0.03	<0.01		88.19†	
	30 May	41.08	<0.01	0.20	8.66	50.43	0.12	0.15	<0.03	<0.01		100.64	
	30 May	39.77	<0.01	0.19	8.38	48.64	0.12	0.14	<0.03	<0.01		97.24	
	1 Jun	40.14	<0.01	0.06	8.21	48.74	0.11	0.01	<0.03	<0.01		97.27	
	1 Jun	40.67	<0.01	0.06	8.42	50.33	0.12	0.01	<0.03	0.01		99.62	
	4 Jun	40.00	0.01	0.14	8.50	49.00	0.12	0.13	<0.03	<0.01		97.90	
	4 Jun	40.06	0.01	0.14	8.58	48.59	0.12	0.12	<0.03	<0.01		97.62	
	7 Jun	39.21	0.01	0.17	8.33	49.22	0.12	0.10	<0.03	<0.01		97.16	
	7 Jun	40.15	0.01	0.17	8.51	48.37	0.12	0.11	<0.03	<0.01		97.44	
	9 Jun	40.59	0.01	0.16	8.66	49.60	0.12	0.12	<0.03	<0.01		99.26	
	9 Jun	40.74	0.01	0.17	8.62	48.05	0.12	0.12	<0.03	<0.01		97.83	
	13 Jun	39.89	0.01	0.17	8.57	48.44	0.12	0.12	<0.03	<0.01		97.32	
	13 Jun	39.87	0.01	0.16	8.66	49.56	0.12	0.11	<0.03	<0.01		98.49	
	14 Jun	39.86	0.02	0.17	8.26	48.31	0.11	0.14	0.03	0.01		96.91	
	14 Jun	39.73	0.01	0.16	8.23	49.47	0.11	0.15	<0.03	0.01		97.87	
	21 Jun	40.56	0.01	0.17	8.48	48.04	0.12	0.09	<0.03	<0.01		97.47	
21 Jun	40.41	0.01	0.18	8.46	48.77	0.12	0.09	<0.03	<0.01		98.04		
Average (wt%):		40.17	0.01	0.15	8.47	48.97	0.12	0.11	0.03	0.01			
Preferred values (wt%):		40.41	0.01	0.19	8.68	49.59	0.12	0.17	0.02	0.001			
Standard deviation (wt%):		0.47		0.04	0.15	0.74		0.04					
Precision (%):		1.17		26.67	1.77	1.51		36.36					
Accuracy (%):		-0.59		-21.05	-2.42	-1.25		-35.29	50.00				

Table T7 (continued).

Standard	Date (2003)	Trace element (ppm)									
		Cr	Ni	Ba	Sr	V	Y	Zr	Sc	Co	Cu
ROA-3*	15 May	1838	1283	90	38	134			28	68	42
	15 May	1876	1424	31	35	140			29	69	43
	26 May	2032	1292	7	36	178	14	27	27	55	53
	30 May	1901	1145	-3	37	183	13	40	29	70	50
	30 May	1875	1140	-2	37	181	13	43	29	68	49
	1 Jun	1952	1169	-1	36	185	14	40	28	72	48
	4 Jun	1921	1206	28	39	185	14	41	30	72	53
	7 Jun	1906	1147	4	36	190	14	39	29	68	55
	9 Jun	1803	1036	-4	37	180	14	40	29	50	51
	13 Jun	1893	1262	-11	40	179	15	38	28	53	51
	14 Jun	1751	1100	-12	38	187	14	40	28	91	56
	21 Jun	1844	1124	-5	38	181	14	40	29	71	52
	Average (wt%):	1883	1194	10	37	175	14	39	29	67	50
	Preferred values (wt%):	1901	1171	1.2	36	192	13	35	28	71	66
	Standard deviation (wt%):	72	105	29	1	18	1	4	1	11	4
	Precision (%):	3.82	8.79	290.00	2.70	10.29	7.14	10.26	3.45	16.42	8.00
Accuracy (%):	-0.96	1.93	88.00	2.70	-9.71	7.14	10.26	3.45	-5.97	-32	
JP-1	15 May	2984	2326	5	0	25			7	107	11
	30 May	3005	2371	12	1	26	1	7	7	115	18
	30 May	3013	2542	15	1	25	0	7	7	111	18
	1 Jun	3080	2449	-13	0	24	0	8	7	114	18
	1 Jun	2910	2220	19	0	26	0	7	7	114	18
	4 Jun	2980	2442	13	2	25	-1	8	7	110	18
	4 Jun	3006	2545	11	3	26	0	7	7	113	18
	7 Jun	3130	2521	26	2	27	0	6	7	107	17
	7 Jun	2945	2461	15	2	25	0	7	7	117	17
	9 Jun	3017	2411	23	1	25	0	7	7	115	18
	9 Jun	3121	2340	4	0	26	-1	7	7	134	18
	13 Jun	3102	2595	0	3	25	1	7	7	110	18
	13 Jun	3055	2437	-1	3	29	1	7	7	101	18
	14 Jun	2926	2366	15	2	26	0	6	7	85	17
	14 Jun	2866	3058	-9	1	26	0	7	7	67	17
	21 Jun	3013	2427	6	2	27	0	8	7	108	18
21 Jun	2983	2548	18	1	26	0	7	7	114	18	
Average (wt%):	3008	2474	9	1	26	0	7	7	108	17	
Preferred values (wt%):	2970	2460	17		29		6.30	7.07	116	49.1	
Standard deviation (wt%):	73	178	11	1	1	0.4	0.6	0.0	14	2	
Precision (%):	2.46	7.19	116.08		3.85	689.63	8.57		12.96	11.76	
Accuracy (%):	1.26	0.57	-88.89		-11.54		10.00	-1	-7.41	-188.82	
DTS-1	26 May	3984	2358	-7	1	0	0	6	3	87	22
	30 May	3979	2244	6	1	12	0	1	3	134	18
	30 May	3939	2479	7	1	11	0	4	3	134	18
	1 Jun	3889	2314	55	1	7	0	0	3	127	18
	1 Jun	3998	2293	7	0	8	0	3	3	133	18
	4 Jun	3978	2310	6	1	9	0	2	3	127	18
	4 Jun	3967	2337	4	1	8	0	3	3	135	18
	7 Jun	4016	2256	-3	1	12	0	3	3	123	17
	7 Jun	3863	2392	-12	2	10	0	2	3	134	17
	9 Jun	3957	2383	-6	0	9	1	2	3	133	18
	9 Jun	4058	2266	-6	0	7	0	3	4	179	18
	13 Jun	3888	2197	30	-2	10	0	3	3	137	18
	13 Jun	4100	2659	-13	2	8	2	2	3	117	18
	14 Jun	3810	2279	55	-1	10	-1	3	3	84	17
	14 Jun	3645	2449	2	-3	10	-1	3	3	114	17
	21 Jun	4023	2299	-1	-4	11	-1	2	3	130	18
21 Jun	3916	2362	17	-3	12	-1	1	3	130	18	
Average (wt%):	3942	2346	8	0	9	0	3	3	127	18	
Preferred values (wt%):	3990	2360	1.70	0.32	11	0.04	4	3.5	137	7.1	
Standard deviation (wt%):	105	109	21	2	3	1	1			1	
Precision (%):	2.66	4.65	262.50		33.33		33.33			5.56	
Accuracy (%):	-1.2	-0.59	370.59		-18.18		-25	-14.29	-7.3	153.52	

Table T7 (continued).

Standard	Date (2003)	Major element oxide (wt%)										Total
		SiO ₂	TiO ₂	Al ₂ O ₃	Fe ₂ O ₃	MgO	MnO	CaO	Na ₂ O	K ₂ O	P ₂ O ₅	
147-895D-10W	15 May	43.92	0.35	3.41	9.86	36.05	0.13	3.52	0.45	0.07		97.76
	15 May	45.19	0.40	3.65	9.82	36.07	0.13	3.69	0.49	0.04		99.48
	Average (wt%)	44.56	0.38	3.53	9.84	36.06	0.13	3.61	0.47	0.06		98.64
	Preferred values (wt%)	43.95	0.49	3.99	12.02	34.88	0.17	3.83	0.56	0.06	0.06	99.95
	Standard deviation (wt%)	0.90	0.04	0.17	0.03	0.01		0.12	0.03	0.02		
	Precision (%)	2.02	10.53	4.82	0.30	0.03		3.32	6.38	33.33		
	Accuracy (%)	1.39	-22.45	-11.53	-18.14	3.38	-23.53	-5.74	-16.07			
BIR-1*	26 May	49.32	0.93	15.01	11.87	9.53	0.17	13.10	1.75	0.03	0.07	101.78
	26 May	48.46	1.01	16.28	11.48	9.65	0.17	13.37	1.93	0.03	0.06	102.44
	30 May	48.00	0.94	15.59	11.34	10.06	0.18	13.31	1.80	0.02		101.24
	1 Jun	47.84	0.93	15.68	11.42	9.81	0.17	13.41	1.81	0.02		101.09
	4 Jun	47.20	0.96	15.31	11.45	9.52	0.17	13.19	1.79	0.02		99.61
	7 Jun	47.38	0.94	15.67	11.18	9.63	0.17	12.93	1.79	0.02		99.71
	9 Jun	46.59	0.93	15.53	11.07	9.51	0.18	13.25	1.82	0.04		98.92
	13 Jun	46.85	0.94	15.32	11.37	9.63	0.17	12.74	1.87	0.02		98.91
	14 Jun	45.57	0.92	15.64	10.94	9.91	0.17	13.01	1.83	0.02		98.01
	21 Jun	47.67	0.94	15.57	11.20	9.66	0.17	13.09	1.82	0.03		100.15
	Average (wt%)	48.59	0.96	15.63	11.56	9.75	0.17	13.26	1.83	0.03	0.07	
	Preferred values (wt%)	47.96	0.96	15.50	11.30	9.70	0.18	13.30	1.82	0.03	0.02	
	Standard deviation (wt%)	0.67	0.04	0.64	0.27	0.28	0.01	0.14	0.09	0.01	0.007	
	Precision (%)	1.38	4.17	4.09	2.34	2.87	5.88	1.06	4.92	33.33	10.00	
Accuracy (%)	1.31		0.84	2.30	0.52	-5.56	-0.3	0.55		250.00		
BHVO-2	15 May	49.86	2.73	13.20	12.26	7.04	0.17	11.29	2.21	0.52		99.28
	26 May	49.81	2.73	13.33	11.97	6.96	0.17	10.90	2.20	0.52	0.25	98.84
	30 May	50.27	2.73	13.45	12.22	7.38	0.17	11.48	2.24	0.52		100.46
	1 Jun	50.16	2.73	13.52	12.28	7.30	0.17	11.48	2.26	0.52		100.42
	4 Jun	49.92	2.74	13.44	12.48	7.25	0.17	11.51	2.23	0.52		100.26
	7 Jun	49.38	2.73	13.40	12.31	7.38	0.17	11.42	2.22	0.52		99.53
	9 Jun	49.15	2.73	13.45	12.31	7.21	0.17	11.53	2.21	0.52		99.28
	13 Jun	49.44	2.74	13.51	12.27	7.26	0.17	11.44	2.18	0.52		99.53
	14 Jun	48.86	2.74	13.64	11.82	7.25	0.16	11.43	2.23	0.52		98.65
	21 Jun	50.06	2.73	13.44	12.23	7.16	0.17	11.46	2.24	0.52		100.01
	Average (wt%)	49.69	2.73	13.44	12.22	7.22	0.17	11.39	2.22	0.52	0.25	
	Preferred values (wt%)	49.90	2.73	13.50	12.30	7.23	0.17	11.40	2.22	0.52	0.27	
Standard deviation (wt%)	0.46	0.005	0.12	0.19	0.14	0.003	0.19	0.02	0.00			
Precision (%)	0.93	0.18	0.89	1.55	1.94	1.76	1.67	0.90				
Accuracy (%)	-0.42		-0.44	-0.65	-0.14		-0.09			-7.41		

Notes: * = run as an unknown. † = due to bad data quality, this value (May 26) was not included in the average. All elements were analyzed at 4000-fold dilution. The obtained values were compared to values for international reference rocks and laboratory standards to assess accuracy and precision. Preferred values are from Puchelt et al. (1996) for Sample 147-895D-10W, Rimaïdi (1993) for ROA-3, Govindaraju (1994) for JP-1, and USGS (2003) for U.S. Geological Survey Reference Materials DTS-1, BIR-1, and BHVO-2. NA = not applicable (no preferred value reported). This table is also available in [ASCI](#).

Table T7 (continued).

Standard	Date (2003)	Trace element (ppm)									
		Cr	Ni	Ba	Sr	V	Y	Zr	Sc	Co	Cu
147-895D-10W	15 May	2415	2846	33	236	89			16	98	26
	15 May	2234	2393	-9	256	101			16	94	28
	Average (wt%):	2325	2620	12	246	95					27
	Preferred values (wt%):	2162	1635	10	184	160			15	86	30
	Standard deviation (wt%):	128	320	29	14	8					1
	Precision (%):	5.51	12.21	246.95	5.69	8.42					3.70
	Accuracy (%):	7.54	60.24	18.41	33.70	-40.63					-10
BIR-1*	26 May	384	181	62	107	308	16	11	43	45	65
	26 May	452	195	1	110	325	17	10	46	47	69
	30 May	387	203	17	108	314	11	18	44	53	61
	1 Jun	370	174	-18	106	313	16	18	43	55	58
	4 Jun	389	187	23	106	324	16	16	45	56	64
	7 Jun	360	188	9	99	319	16	17	44	50	68
	9 Jun	353	197	4	105	312	16	18	44	65	63
	13 Jun	352	179	2	109	308	17	16	45	47	64
	14 Jun	341	288	-11	107	311	15	16	44	47	70
	21 Jun	364	172	1	108	319	16	15	45	54	63
	Average (wt%):	408	193	27	108	316	15	13			65
	Preferred values (wt%):	370	170	6	110	310	16	18	44	52	125
	Standard deviation (wt%):	38	11	32	2	9	3	4			4
	Precision (%):	9.31	5.70	118.52	1.85	2.85	20.00	30.77			6.15
	Accuracy (%):	10.27	13.53	350.00	-1.82	1.94	-6.25	-27.78			1.94
BHVO-2	15 May	290	79	130	389	320			31	62	133
	26 May	284	122	169	390	26	130	311	31	51	148
	30 May	271	142	130	390	312	26	172	31	58	148
	1 Jun	278	114	115	390	310	26	172	32	59	148
	4 Jun	279	116	130	391	315	26	172	32	62	148
	7 Jun	267	132	129	391	305	26	172	32	64	149
	9 Jun	254	230	127	389	314	26	172	32	63	149
	13 Jun	262	150	123	390	312	26	172	32	58	148
	14 Jun	268	195	95	391	314	25	172	31	68	166
	21 Jun	270	117	130	390	311	26	172	32	63	148
	Average (wt%):	272	140	128	390	284	37	187			149
	Preferred values (wt%):	280	119	130	389	317	26	172	32	45	127
	Standard deviation (wt%):	11	44	18	1	91	35	46			8
	Precision (%):	4.04	31.43	14.06	0.26	32.04	94.59	24.60			5.37
Accuracy (%):	-2.86	17.65	-1.54	0.26	-10.41	42.31	8.72			17.32	

Table T8. Estimates of accuracy and precision for Carlo Erba gas chromatography analyses of CO₂, H₂O, and S.

Standard	Date (2003)	Volatiles		
		CO ₂ (wt%)	H ₂ O (wt%)	S (ppm)
JP-1	23 May	0.31	3.04	
	27 May		2.39	
	28 May	0.30	2.94	
	31 May	0.29	2.73	
	5 Jun	0.30	2.95	
	10 Jun	0.33	3.05	
	13 Jun	0.33	3.21	
	16 Jun	0.32	2.43	
	21 Jun	0.36	2.32	
	Average (wt%):	0.32	2.79	
	Preferred value (wt%):		3	
	Standard deviation (wt%):	0.02	0.33	
	Precision (%):	7.00	11.74	
Accuracy (%):	NA	0.55		
BAS140	23 May	0.12	1.20	841
	27 May		1.42	
	28 May	0.12	1.05	1237
	31 May	0.11	1.06	929
	5 Jun	0.11	1.12	546
	10 Jun	0.13	1.16	1479
	13 Jun	0.11	1.26	628
	16 Jun	0.13	1.93	493
	21 Jun	0.16	1.78	581
	Average (wt%):	0.12	1.33	842
	Preferred value (wt%):	0.05	1.12	900
	Standard deviation (wt%):	0.02	0.32	357
	Precision (%):	12.86	24.00	42.42
Accuracy (%):	58.79	15.90	-6.93	
147-895D-10W	23 May	0.98	10.76	
	27 May	0.88	10.43	
	28 May	1.08	11.03	
	31 May	1.05	11.33	
	5 Jun	0.92	11.66	
	10 Jun	1.41	11.36	
	13 Jun	1.09	13.78	
	16 Jun	0.97	9.99	
	21 Jun	1.14	11.14	
	Average (wt%):	1.06	11.28	
	Preferred value (wt%):	0.95	9.62	600
	Standard deviation (wt%):	0.16	1.07	
	Precision (%):	14.84	9.48	
Accuracy (%):	11.24	17.23		

Notes: Preferred values: BAS140 (Sparks and Zuleger, 1995), JP-1 (Sims et al., 1988), and 147-895D-10W (Puchelt et al, 1996). NA = not applicable (no preferred value). This table is also available in [ASCII](#).

Table T9. Magnetic data for discrete sample standards.

Standard*	Vector average				Accepted values			Deviation	
	Declination (°)	Inclination (°)	Intensity (Am ²)	CSD	Declination (°)	Inclination (°)	Intensity (Am ²)	Angle (°)	Intensity (%)
2	211.5	59.7	1.566E-07	5.6	209.9	59.6	1.54E-07	0.82	1.66
3	106.0	-33.1	2.439E-08	6.8	101.7	-33.3	2.40E-08	3.63	1.61
4	339.1	-3.2	6.181E-06	7.5	335.8	-3.7	6.17E-06	3.29	0.18
5	49.8	-52.0	4.447E-06	5.8	47.0	-52.6	4.35E-06	1.82	2.24
6	206.2	-3.8	1.008E-07	7.1	203.8	-3.6	1.01E-07	2.40	-0.24
8	186.0	27.9	2.508E-06	6.7	183.8	27.9	2.49E-06	1.93	0.74
							Average:	2.32	1.29
							Standard deviation:	1.03	0.82

Notes: * = standards from interlaboratory calibration for Time Averaged Field Initiative (TAFI) (Tauxe, pers. comm., 2001). Accepted values based on measurements from multiple U.S. laboratories. CSD = crystal size distribution. This table is also available in [ASCII](#).

Table T10. Discrete sample standard data after tray repositioning.

Standard	Position	Vector average			Deviation*	
		Declination (°)	Inclination (°)	Intensity (Am ²)	Angle (°)	Intensity (%)
2	1	209.6	59.8	1.56718E-07	0.25	1.76
2	2	209.0	59.7	1.57156E-07	0.47	2.05
2	3	209.5	59.6	1.55866E-07	0.18	1.21
2	4	209.9	59.5	1.55617E-07	0.08	1.05
2	5	210.1	60.2	1.54817E-07	0.65	0.53
3	1	103.5	-33.1	2.46212E-08	1.53	2.59
3	2	104.0	-33	2.44948E-08	1.99	2.06
3	3	104.0	-33.4	2.45891E-08	1.91	2.45
3	4	103.8	-32.9	2.43558E-08	1.79	1.48
3	5	102.0	-34.1	2.40099E-08	0.90	0.04
4	1	336.4	-3.3	6.26312E-06	0.70	1.51
4	2	336.2	-3.1	6.27177E-06	0.74	1.65
4	3	336.3	-3.0	6.23101E-06	0.87	0.99
4	4	336.4	-3.1	6.21612E-06	0.85	0.75
4	5	336.2	-3.6	6.20086E-06	0.37	0.50
6	1	204.0	-2.5	1.00844E-07	1.13	-0.15
6	2	203.7	-2.4	1.01805E-07	1.24	0.80
6	3	203.5	-3.0	1.01223E-07	0.70	0.22
6	4	203.2	-2.9	1.00963E-07	0.89	-0.04
6	5	204.9	-1.2	9.98525E-08	2.64	-1.14

Notes: * = angular and intensity deviations are relative to accepted values given in Table T9, p. 71. This table is also available in ASCII.

Table T11. Measurements and specifications for wireline tool strings and LWD tools.

Tool string	Logging speed (m/hr)	Tool	Measurement	Tool length (m)	Sampling interval (cm)	Approximate vertical resolution (cm)	Maximum temperature (°C)
Triple combination	488	HNGS	Spectral gamma ray	2.59	15	51	260
		APS	Porosity	3.96	5 and 15	43	175
		HLDS	Bulk density, photoelectric factor	7.03	2.5 and 15	38	175
		DIT	Resistivity	9.53	15	76, 150, 200	175
		TAP	Temperature	2.71	1 per s	NA	105
			Tool acceleration		4 per s	NA	
Pressure			1 per s	NA			
Formation MicroScanner (FMS)-sonic combination	250	FMS	Microresistivity	7.72	0.25	0.5	175
		GPIT	Tool orientation	(in FMS)	0.25 and 15	NA	175
		SGT	Total gamma ray	4.52	15	NA	175
		DSI	Acoustic velocity	15.5	15	107	175
LWD		RAB	Resistivity image	3.08	1/10 s	5–8	150
			Gamma ray		1/10 s	46	

Notes: All tool and tool string names (except the TAP) are trademarks of Schlumberger. For the complete list of acronyms used in the ODP and for additional information about tool physics and use consult ODP Logging Services at www.ldeo.columbia.edu/BRG/ODP. See Table T12, p. 74, for explanation of acronyms used to describe tool string and tools. NA = not applicable. LWD = logging while drilling. RAB = resistivity at the bit.

Table T12. Acronyms and units used for wireline logging tools.

Tool	Output	Tool/Measurement	Unit
APS		Accelerator Porosity Sonde	
	APLC	Near array porosity (limestone calibrated)	%
	FPLC	Far array porosity (limestone calibrated)	%
	SIGF	Formation capture cross section (Σf)	Capture units
	STOF	Tool standoff (computed distance from borehole wall)	in
DIT		Dual Induction Tool	
	IDPH	Deep induction resistivity	Ωm
	IMPH	Medium induction resistivity	Ωm
	SFLU	Spherically focused resistivity	Ωm
DSI		Dipole Sonic Imager	
	DTCO	Compressional wave delay time (Δt)	ms/ft
	DTSM	Shear wave delay time (Δt)	ms/ft
	DTST	Stoneley wave delay time (Δt)	ms/ft
FMS		Formation MicroScanner	
	C2, C2	Orthogonal hole diameter	in
	P1AZ	Pad 1 azimuth Spatially oriented resistivity images of borehole wall	Degrees
GPIT		General Purpose Inclinator Tool	
	DEVI	Hole deviation	Degrees
	HAZI	Hole azimuth	Degrees
	F_x, F_y, F_z A_x, A_y, A_z	Earth's magnetic field (three orthogonal components) Acceleration (three orthogonal components)	Oersted m/s^2
HLDS		Hostile Environment Litho-Density Sonde	
	RHOM	Bulk density	g/cm^3
	PEFL	Photoelectric effect	b/e ⁻
	LCAL	Caliper (measure of borehole diameter)	in
	DRH	Bulk density correction	g/cm^3
HNGS		Hostile Environment Gamma Ray Sonde	
	HSGR	Standard (total) gamma ray	gAPI
	HCGR	Computed gamma ray (HSGR minus uranium contribution)	gAPI
	HFK	Potassium	wt%
	HTHO	Thorium	ppm
	HURA	Uranium	ppm
SGT		Scintillation Gamma Ray Tool	
	GR	Total gamma ray	gAPI
	ECGR	Environmentally corrected gamma ray	gAPI
	EHGR	High-resolution environmentally corrected gamma ray	gAPI
TAP		Temperature/Acceleration/Pressure Tool	$^{\circ}C, mm/s^2, psi$

Notes: All tool and tool string names (except the TAP) are trademarks of Schlumberger. For the complete list of acronyms used in the ODP and for additional information about tool physics and use consult ODP Logging Services at www.ldeo.columbia.edu/BRG/ODP.

Table T13. Photoelectric effect of igneous and alteration minerals associated with lower crustal and upper mantle environments.

	Mineral	Composition	P_e
Clay	Kaolinite	$Al_4[Si_4O_{10}](OH)_8$	1.49
	Illite	$KAl_4[Si_7AlO_{26}](OH)_4$	2.05
	Chlorite	$Mg_{12}[(Si, Al)_8O_{20}](OH)_{16}$	1.40
	Quartz	SiO_2	1.81
	Chlorite	$Mg_{12}[(Si, Al)_8O_{20}](OH)_{16}$	1.40
	Spinel	$MgAl_2O_4$	1.49
	Serpentine	$Mg_3[Si_2O_5](OH)_4$	1.40
	Biotite	$K_2Mg_6[Si_6Al_2O_{20}](OH)_4$	2.30
	Calcite	$CaCO_3$	5.08
Amphibole	Pargasite	$NaCa_2Mg_4Al_3Si_6O_{22}(OH)_2$	2.55
	Tremolite	$Ca_2Mg_5Si_8O_{22}(OH)_2$	2.62
	Hornblende	$Ca_2Fe^{+3}_3[Si_6Al_2O_{22}](OH)_2$	10.49
Fe-Ti oxide	Ilmenite	$Fe^{+2}Ti^{+4}O_3$	16.63
	Hematite	Fe_2O_3	21.48
	Magnetite	$Fe^{+2}Fe^{+3}_2O_4$	22.24
Olivine	Forsterite	Mg_2SiO_4	1.54
	Fayalite	Fe_2SiO_4	17.17
Pyroxene	Orthopyroxene	$MgSiO_3$	1.84
	Clinopyroxene	$CaMgSi_2O_6$	3.53
	Augite	$Mg_2(SiAl)_2O_6$	4.69
	Orthoferrosilite	$FeSiO_3$	13.57
Feldspar	Albite	$NaAlSi_3O_8$	1.68
	Anorthite	$CaAl_2Si_2O_8$	3.13

$P_e = (Z_e/10)^{3.6}$
 $P_e = (\sum A_i Z_i P_i) / (\sum A_i Z_i)$

Notes: A_i = number of each atom in the molecule. Z_i = atomic number for each element. P_e = photoelectric cross-section index.